Chapter 2
Discrete-Continuous Model of Crystal Plasticity

2.1 Introduction of Simulation Method

With the development of micro and nanotechnology, increasing interest has been placed on investigating the mechanical behavior of submicron materials. As described in Sect. 1.1, numbers of new phenomena in plastic deformation have been observed at small scales, such as size effect [1], strain burst [2, 3] etc. However, the experimental studies alone cannot give full understanding of the underlying mechanism. In recent years, crystal plastic simulation method based on discrete dislocation has gradually become a key tool to supplement experimental testing, and is widely used to explore mechanism that are currently hard to be observed experimentally [4–9].

2.1.1 Discrete Dislocation Dynamics (DDD)

In the three dimensional discrete dislocation dynamics (3D-DDD) simulation method used in this paper, an arbitrary curve dislocation is discrete into several straight dislocation segments [10–14]. As shown in Fig. 2.1, each dislocation segment, which can be of a screw, edge or mixed character, is presented by two connected nodes.

2.1.1.1 Dislocation Kinetic Equation

For an arbitrary dislocation segment i, its kinetic equation obeys the following relationship,

$$\mathbf{M}_{\mathrm{d}}\dot{\mathbf{v}}_i + \mathbf{B}\mathbf{v}_i = \mathbf{f}_i \tag{2.1}$$

Y. Cui, *The Investigation of Plastic Behavior by Discrete Dislocation Dynamics for Single Crystal Pillar at Submicron Scale*, Springer Theses,
DOI 10.1007/978-981-10-3032-1_2

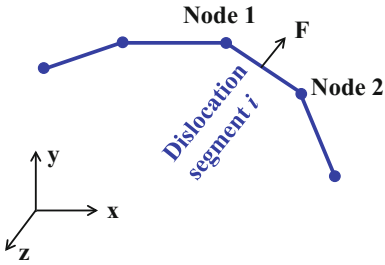

Fig. 2.1 Discreteness of curved dislocation line

where $\mathbf{M}_d$ and $\mathbf{B}$ are the corresponding effective mass matrix and the drag coefficient matrix, respectively. $\mathbf{v}_i$ and $\mathbf{f}_i$ are the nodal velocity vector and nodal force vector, respectively. At room temperature, the dislocation motion is assumed to be in the over-damped regime [15], namely, dislocation velocity can rapidly reach the stable value. Therefore, during the simulation, the first inertia term on the left side of Eq. (2.1) is ignored. Assuming that dislocation mobility is isotropic, $\mathbf{B}$ is expressed as $\mathbf{B} = \int_l B_0 \mathbf{N}^{\mathrm{T}} \mathbf{N} \mathrm{d}l$. Here, $\mathbf{N}$ is shape function, B_0 is static drag coefficient matrix. $\mathbf{f}_i = \int_l \mathbf{N}^{\mathrm{T}} \mathbf{f} \mathrm{d}l$, where $\mathbf{f}$ is the external force vector acting per unit length dislocation line, which is calculated as follows,

$$\mathbf{f} = (\boldsymbol{\sigma}_i \cdot \mathbf{b}_i) \times \boldsymbol{\xi}_i + \mathbf{f}^{\mathrm{self}} + \mathbf{f}^{\mathrm{image}} \tag{2.2}$$

The first term on the right side represents the Peach–Koehler force, where $\boldsymbol{\sigma}_i$ is the stress field caused by other dislocations and external boundary conditions; $\mathbf{b}_i$ is the Burgers vector of segment i; and $\boldsymbol{\xi}_i$ is the unit vector describing its direction. The second term, $\mathbf{f}^{\mathrm{self}}$, is the line tension, which is computed by the negative derivative of the segment total energy with respect to its position. The third term, $\mathbf{f}^{\mathrm{image}}$, is the image force induced by free surface.

Regarding traditional DDD simulations, periodic boundary condition is usually applied, without considering image force. For submicron crystal, the image force induced by free surface plays a very important role in influencing the behavior and evolution of dislocations. The solution by Hirth and Lothe [16] describes the image force induced by dislocation segments with unit length, which is parallel to the free surface,

$$\mathrm{d}F = \frac{1}{\lambda}\left(E(\beta)\tan\alpha + \frac{\partial E(\beta)}{\partial \alpha}\right)\mathrm{d}l, \quad E(\beta) = \frac{\mu b^2(1 - v\cos^2\beta)}{4\pi(1-v)} \tag{2.3}$$

where μ is shear modulus, v is Poisson ratio, the energy term $E(\beta)$ is obtained for isotropic elastic body. Figure 2.2 schematically describes the definitions of angle α and β, as well as the distance λ. Here, the dashed line arrow describes the burgers vector direction. When the dislocation line is very close to the free surface, the image force described by Eq. (2.3) is singular. Liu and Schwarz found that the image force reached an approximate value before becoming divergent [17]. Therefore, the image

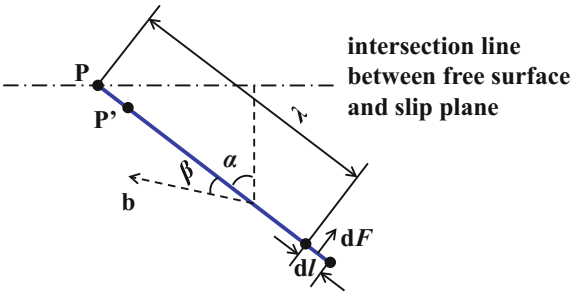

Fig. 2.2 Straight dislocation line intersects with free surface at point P. A view from the normal direction of the slip plane [12]

force at point P in Fig. 2.2 can be taken as the averaged value in this approximation region, which is roughly taken as the value at the closed point P′, to eliminate the singularity.

2.1.1.2 Dislocation Reaction and Topology Update

During each step of DDD, apart from calculating dislocation velocity, the topology also requires to be updated to deal with the short range interactions between dislocations. Generally, some criterions [18] and operators [19] must be given. As shown in Fig. 2.3, these dislocation reactions are achieved through the merge and split operators of the dislocation segment and nodes. According to the relation of the burgers vectors and slip planes of the reaction dislocation segments, the dislocation reactions that can be captured by DDD are mainly classified as follows [20],

(1) Mutual annihilation: Two dislocations of opposite burgers vector direction in the same slip plane;
(2) Collinear annihilation: The burgers vector directions of the two dislocations are collinear. Each dislocation is in the cross-slip plane of the other dislocation;

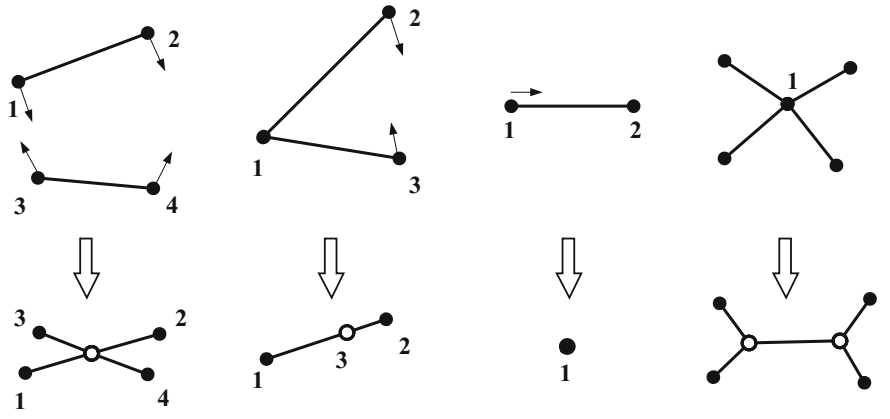

Fig. 2.3 Four main merge and split operators for dislocation segments and nodes

(3) Hirth lock: Two dislocations of perpendicular burgers vector direction in the intersection slip plane;
(4) Glissile junction: The sum of the burgers vectors of two dislocations is parallel to one slip plane. Their slip planes are intersecting;
(5) Lomer lock: The sum of the burgers vectors of two dislocations is not parallel to either slip plane. Their slip planes are intersecting.

In addition, when dislocations glide out of the crystal, the surface annihilation should also be considered as shown in Fig. 2.4.

2.1.1.3 Dislocation Cross Slip

Cross slip has attracted much attention in face-centered cubic crystal (FCC) with medium to high stacking fault energy [21–25]. In a complex dislocation network, cross-slip events can be frequently induced by local heterogeneous stress state [22]. Cross slip significantly affects spatial-temporal developments in dislocation microstructure under both quasi-static and shocking loads [24]. High cross slip activity is inclined to make the substructure morphology appear cellular instead of planar [24], and promote dislocation self-organization instead of rather uniform dislocation distributions [21]. Therefore, it is important to introduce a reasonable cross slip model in DDD simulations.

Numerous models have been built to describe the physical process of cross slip [26]. Generally, screw dislocation will dissociate into a pair of partial dislocations separated by a lattice stacking fault. For most densely packed planes, such as (111) for FCC, dislocation core prefers to extend. The occurrence of cross slip requires the stacking fault ribbon to be compressed to a critical length, either by applied stress or by thermal fluctuations. Then, the dislocations may bow out in the cross slip plane or re-dissociate if the cross-slip plane is a close-packed one [27]. From a simulation point of view, the process of cross slip usually can only be modeled phenomenologically since dislocation core property is involved [28].

In this work, three conditions must be met for the occurrence of cross slip [27]: (i) The resolved shear stress in cross-slip plane should be larger than that in initial glide plane, because cross slip will take energy and hardly happen unless screw dislocations have low mobility in the habit slip plane; (ii) The concerned screw segments should be larger than a restricted length set as 0.1 μm. This corresponds

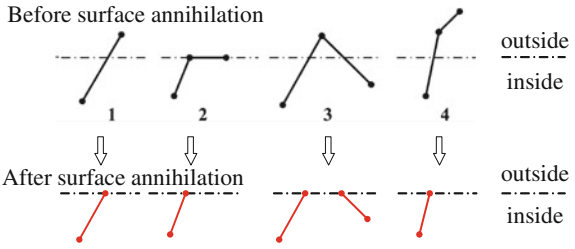

Fig. 2.4 Four possible geometries and the corresponding topology update schemes when dislocations are absorbed at the free surface

to the condition for stacking fault ribbon constriction [28]; (iii) The probability of a cross slip event in each discrete time step is determined by Monte-Carlo method given below [29],

$$P = \beta \frac{L}{L_0} \frac{\delta t}{\delta t_0} \exp\left(V \cdot \frac{\tau - \tau_{\mathrm{III}}}{kT}\right) \tag{2.4}$$

where V is the activation volume, τ_{III} is the resolved shear stress at the onset of stage III during a tension test, k is the Boltzmann constant, L_0 and δt_0 represent length and time, respectively. For aluminum (Al) [30], $V = 300b^3$, b is the burgers vector magnitude, $\tau_{\mathrm{III}} = 5$ MPa, $L_0 = 1$ μm, $\delta t_0 = 1$ s. The probability P is set to one at room temperature by adjusting normalizing coefficient β, when screw dislocation with length $L = L_0$ is subjected to a resolved shear stress $\tau = \tau_{\mathrm{III}}$. Cross slip occurs only when the calculated P is larger than a randomly generated number N between 0 and 1. Actually, if τ is much larger than τ_{III}, the probability function will become inoperative, implying that cross slip is thermally activated.

2.1.2 Coupling DDD with Finite Element Method

Even though DDD simulations can offer significant insights for the microstructure evolution during deformation, DDD modeling alone cannot consider the finite deformation of the computational cell. In addition, it is difficult to deal with complex boundary conditions and surface effect, since it is based on the theoretical solution of stress field for a dislocation in an infinite crystal [11]. To overcome these problems, DDD is usually coupled with finite element methods (FEM) [12, 31–33] or boundary element methods [34, 35], respectively. These coupling procedures can be mainly divided into two categories: one is superposition method (SPM), and the other is so called discrete-continuous model (DCM). In the following, only the streamlined presentations of the framework for these two methods are described for completeness. Details of the methods are described elsewhere [11, 12, 31–33, 35–38].

2.1.2.1 Superposition Method (SPM)

SPM is first proposed by Van der Giessen and Needleman [32]. As schematically shown in Fig. 2.5a, the total stress field $\boldsymbol{\sigma}$ in a finite crystal medium is the sum of analytical stress field of dislocations in an infinite media $\boldsymbol{\sigma}^{\infty}$ and a complementary elastic solution $\widehat{\sigma}$,

$$\boldsymbol{\sigma} = \boldsymbol{\sigma}^{\infty} + \widehat{\sigma} \tag{2.5}$$

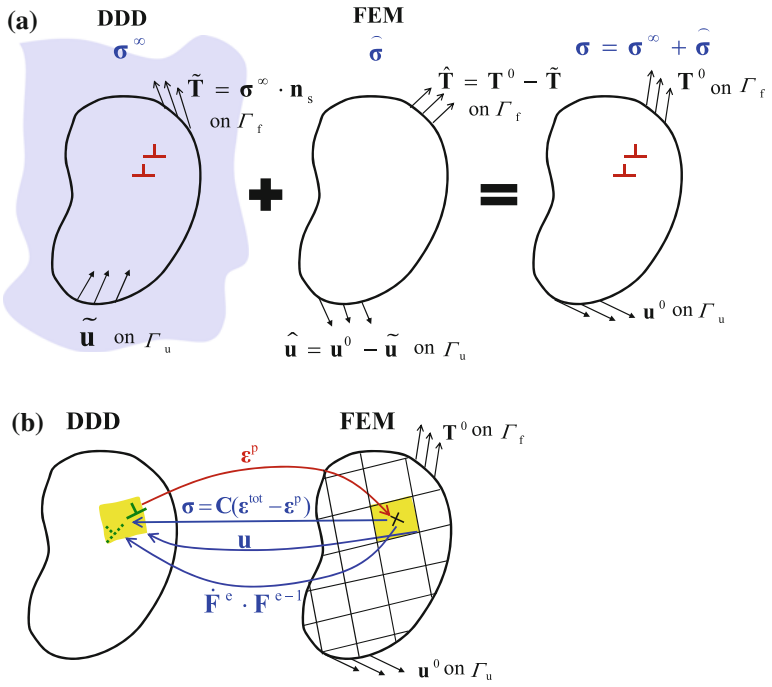

Fig. 2.5 **a** Schematic diagram of SPM [32]; **b** schematic of variable-transferring procedures in improved DCM. Reprinted from Ref. [41], Copyright 2015, with permission from Elsevier

$\boldsymbol{\sigma}^{\infty}$ is generally obtained by analytical solution, which will induce surface traction on the sample,

$$\tilde{\mathbf{T}} = \boldsymbol{\sigma}^{\infty} \cdot \mathbf{n}_s \tag{2.6}$$

Here, $\mathbf{n}_s$ is the normal direction of surface. Complementary stress field is used to cancel this surface traction and consider the real boundary condition.

The short range interaction can be relatively well captured by SPM [37]. However, the analytical stress fields of all dislocations must be recalculated at each time step, which requires extensive computing time. Besides, it is relative complicated to deal with anisotropic media [39] and biomaterial [40]. More importantly, the concept of 'plastic strain' is not explicitly introduced.

2.1.2.2 Discrete-Continuous Model (DCM)

DCM is based on the concept of 'eigenstrain' in micromechanics, which can directly calculate the plastic strain and solve the boundary value problem under a unified framework [36, 38]. In previous work [11, 12], it mainly contains the

following three information-transfer procedures as shown in Fig. 2.5b: (i) Calculating the plastic strain $\boldsymbol{\varepsilon}^{\mathrm{p}}$ induced by the glide of dislocations using DDD simulation. Then, the plastic strain is localized to the continuum material point, which is crucial in the whole calculation procedure. This replaces the conventional phenomenological constitutive law to calculate the total stress,

$$\overset{\nabla}{\boldsymbol{\sigma}}^{e} = \mathbf{C}^{\mathrm{e}} : (\dot{\varepsilon} - \dot{\varepsilon}^{\mathrm{p}}) \tag{2.7}$$

where $\overset{\nabla}{\boldsymbol{\sigma}}^{\mathrm{e}}$ is the Jaumann rate of Cauchy stress $\boldsymbol{\sigma}$, $\mathbf{C}^{\mathrm{e}}$ is the tensor of elastic modulus, $\dot{\varepsilon}$ is the total strain rate tensor. (ii) The equilibrium stress field associated with the homogenized plastic strain is calculated by FEM under a specific boundary condition in a unified continuum mechanics framework. It is expressed as follows [11, 12],

$$\mathbf{M}\ddot{\mathbf{u}} + \mathbf{f}^{\mathrm{int}} = \mathbf{f}^{\mathrm{ext}} \tag{2.8}$$

$$\begin{aligned} \mathbf{M} &= \int_{\Omega} \rho \mathbf{N}^{\mathrm{T}} \mathbf{N} \mathrm{d}\Omega \\ \mathbf{f}^{\mathrm{int}} &= \int_{\Omega} \mathbf{B}_{\mathrm{e}}^{T} \boldsymbol{\sigma} \mathrm{d}\Omega \\ \mathbf{f}^{\mathrm{ext}} &= \int_{\Gamma} \mathbf{B}_{\mathrm{e}}^{T} \mathbf{T}^{0} \mathrm{d}\Gamma + \int_{\Omega} \mathbf{B}_{\mathrm{e}}^{T} \boldsymbol{\sigma}^{0} \mathrm{d}\Omega \end{aligned} \tag{2.9}$$

$$\begin{aligned} &\mathbf{u} = \mathbf{u}^{0} \quad \Gamma \in \Gamma_{\mathrm{u}} \\ &\mathbf{T} = \mathbf{T}^{0} \quad \Gamma \in \Gamma_{\mathrm{f}}, \quad \mathbf{T} = 0 \; \Gamma \notin (\Gamma_{\mathrm{u}} \cup \Gamma_{\mathrm{f}}) \end{aligned} \tag{2.10}$$

where $\mathbf{M}$ is mass matrix, $\mathbf{N}$ is shape function, $\mathbf{B}_{\mathrm{e}} = \mathrm{grad}[\mathbf{N}]$, $\mathbf{f}^{\mathrm{int}}$ is an internal force and $\mathbf{f}^{\mathrm{ext}}$ is an external force resulting from the applied traction $\mathbf{T}^{0}$ and initial stress field $\boldsymbol{\sigma}^{0}$, which is introduced to represent the preexisting stationary dislocations. Then, the stress field $\boldsymbol{\sigma}$ calculated by FEM is transferred to DDD and serves as the applied stress to drive dislocation motion; (iii) The displacement field $\mathbf{u}$ of FEM cell is transferred into DDD cell to update the geometry configuration. In DCM, the time increment Δt_{DDD} in DDD model is set to be a very small value (10^{-10}–10^{-12} s), which can be equal to or smaller than that in the FEM model.

Even though both DCM and SPM have been largely investigated in recent years [31, 36, 37, 40], there are still some important problems that are not well clarified yet, especially for DCM. The present work will mainly focus on DCM with respect to the following critical issues. The key to DCM is the 'regularization method' used to localize the discrete plastic strains to continuum material points. Different researchers have proposed various regularization methods [12, 36–38]. However, a quantitative comparison among them and how to select the slip system dependent

adjustment parameters are still not clear. The second key issue is the calculation of the so called 'image force'. At small scales, the image force caused by free surface attracts the dislocations toward the surface and thus promotes dislocation starvation [42], trigger cross slip of surface dislocation [4] etc. In order to investigate submicron plasticity, special attention must be paid to the dislocation image force calculation. Generally, SPM is supposed to effectively capture the short-range interaction and image force effect. Thus, SPM and DCM are sometimes used together in the multiscale model with the aim of taking full advantage of both methods [11, 38]. However, whether will this kind of treatment double-count the contribution of the image force? How accuracy can DCM alone capture the effect of free surface? There are still no efforts in these aspects reported in the literatures till now even though these studies can provide useful guidelines for effectively correcting the image force calculation in DCM. The third key issue is the reproduction of deformed configuration in DCM, especially for the analysis of failure process. In the micropillar compression experiments, the deformation is usually observed to be localized in a few slip bands [43, 44] (see Fig. 2.6). This leads to significant variations in surface configuration, and further influences their stress distribution and failure process. For example, small variation in a surface configuration can lead to stress concentration sufficient to promote crack initiation. Deshpande et al. [45] proposed the finite deformation discrete dislocation plasticity calculation framework based on 2D-DDD. El-Awady et al. [35] coupled DDD and boundary element method to investigate the deformed shape of micropillar induced by the operation of Frank-Read sources. Zbib et al.'s simulation work also reproduced the character of deformation bands and the formation of ledges on the surface [38, 46]. Gao et al. [11] captured the buckling configuration when the micropillar is subjected to uniaxial compression without friction between the pillar and the indenter. However, the algorithmic details to capture deformed configuration have not been given, and very few attempts have been made to quantitatively study how DCM performs on

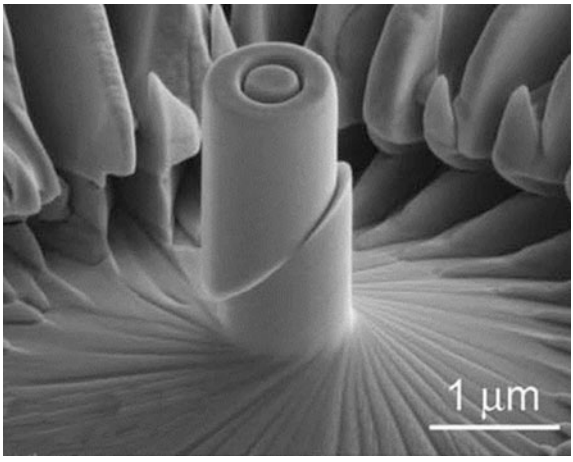

Fig. 2.6 Scanning electron microscope image showing the surface morphology of micropillar with diameter 1 μm after compression [44]

reproducing the deformed configuration. Moreover, little efforts have been made to directly consider the lattice rotation in 3D-DDD model, which limits DCM model to tackle truly finite-strain problems. The next section is aimed at addressing these issues through several typical numerical tests.

2.2 Improved Discrete-Continuous Model

2.2.1 Efficient Regularization Method

In this section, different regularization methods proposed by previous researchers are briefly reviewed. A new regularization method is proposed to combine the advantages of previous regularization methods. In order to validate all these methods, the calculated stress field of one prismatic dislocation loop is compared with analytical solution.

As shown in Fig. 2.7, supposing a dislocation segment AB slips to A′B′ without rotating during a time increment, the swept area is S_{AB}. According to Orowan's law, the total plastic shear increment $\Delta\gamma$ can be explicitly expressed as a function of the area swept by dislocation motion,

$$\Delta\gamma = \frac{bS_{AB}}{V} \tag{2.11}$$

where b is a magnitude of Burgers vector, V is representative volume. This plastic strain increment will be localized to the material points (or integration points) of FEM element around the swept area by some regularization methods.

At the center of swept surface, a local coordinate system can be established as shown in Fig. 2.7, where **n** is the normal direction of slip plane, **g** is the glide direction, and **ξ** is the dislocation line direction. From a view along **ξ** direction, the different regularization methods are schematically presented in Fig. 2.8. Actually, the main differences between different regularization methods reside in the choice of representative volume V in Eq. (2.11) and the way of distributing total plastic shear increment $\Delta\gamma$ to the multiple integration points.

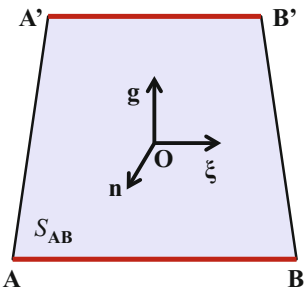

Fig. 2.7 Dislocation segment AB glides to A′B′, generating swept surface S_{AB}, a local coordinate system is built at the center of S_{AB}

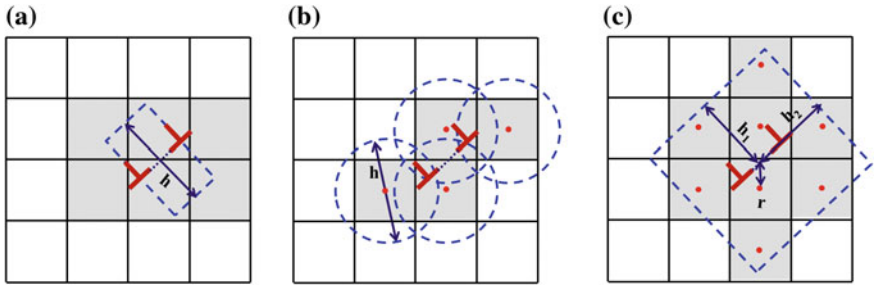

Fig. 2.8 Plastic strain induced by dislocation glide is localized in the shaded elements with different methods, **a** used by Lemarchand et al. [36], **b** used by Vattré et al. [37], and **c** used by Liu et al. [12]. The *red points* in (**b**) and (**c**) represent the integration points, and linear element is used for clarity of presentation. Reprinted from Ref. [41], Copyright 2015, with permission from Elsevier

2.2.1.1 Review of Different Regularization Methods

Most previous studies take V in Eq. (2.11) as the elementary volume V^{int} associated with each integration point in the FEM element [12, 36]. In this case, the total plastic shear increment $\Delta\gamma$ is expressed as $\Delta\gamma^{\text{int}} = bS_{AB}/V^{\text{int}}$.

The first typical regularization method is proposed by Lemarchand et al. [36]. Based on the Volterra-like procedure, as discussed by Mura [47], the elementary slip events in the glide plane is extended over a slab of finite thickness h (see Fig. 2.8a). Physically speaking, in this method, dislocation AB and A′B′ are considered as plate-like inclusion with cross section area equal to the swept area S_{AB} and thickness equal to h. The total plastic shear increment $\Delta\gamma^{\text{int}}$ is then localized to each integration point according to the intersection volume $\Delta V_{\text{s}}^{(i)}$ between the sheared slab and elementary volume V^{int},

$$\Delta\gamma^{(i)} = \frac{\Delta V_{\text{s}}^{(i)}/h}{S_{\text{AB}}} \cdot \Delta\gamma^{\text{int}} \tag{2.12}$$

Hereafter, the superscript "(i)" means the variables associated with the ith integration point. $\Delta V_{\text{s}}^{(i)}/h$ can be considered as an effective area corresponding to the ith integration point.

Recently, Vattré et al. [37] presented the algorithmic details of the regularization procedure, and make some improvement with respect to Lemarchand et al.'s work. In their work, the elementary slip event is also considered as plate-like inclusion surrounding its swept surface, but the inclusion is further thought of as the union of overlapping elementary spheres with diameter h. They takes V in Eq. (2.11) as the volume of the representative sphere V^{sphere}, and the total plastic shear increment $\Delta\gamma$ is expressed as $\Delta\gamma^{\text{sphere}} = bS_{AB}/V^{\text{sphere}}$. Each sphere centers within the swept surface and corresponds to a homogeneously distributed plastic shear increment.

Once an integration point is located within one or more elementary sphere, its plastic shear increment is non-zero. This procedure can be equivalent to the following process. Considering a sphere with center at the ith integration point and diameter equal to h as shown in Fig. 2.8b, the plastic shear increment at each integration point is calculated according to the intersection area between this sphere and the swept surface $S^{(i)}_{\text{sphere}}$,

$$\Delta\gamma^{(i)} = \frac{S^{(i)}_{\text{sphere}}}{S_{\text{AB}}}\Delta\gamma^{\text{sphere}} \tag{2.13}$$

The form of Eq. (2.13) seems similar to Eq. (2.12). However, in Eq. (2.12), the parameter h is introduced during the localization process, while in Eq. (2.13), h is used to calculate the representative volume. The use of spherical shape makes it convenient to treat the problems with internal interfaces [37]. However, the sum of the localized plastic strain increment $\sum_i \Delta\gamma^{(i)}$ for all the elements participating regularization is not as straightforward as other methods, because some swept area may be included in two or more elementary spheres.

Different from the regularization methods above, Liu et al. [12] localized the total plastic shear increment $\Delta\gamma^{int}$ according to a weight function $w^{(i)}$,

$$\Delta\gamma^{(i)} = \frac{w^{(i)}}{\sum_{i=1}^{n} w^{(i)}}\Delta\gamma^{\text{int}} \tag{2.14}$$

where n is the total number of integration points whose weight function is non-zero. The weight function is expressed as a function of isotropic Burgers vector density function $\omega(r)$, based on the non-singular continuum theory of dislocations developed by Cai et al. [48],

$$w^{(i)} = \int_{V^i} \omega(\mathbf{x})dV, \quad \omega(r) = \frac{1}{\pi}\frac{a}{r^2 + a^2} \tag{2.15}$$

where V^i is the volume occupied by the ith integration point, a is a spreading radius, r is the distance between an integration point and the center of swept surface as shown in Fig. 2.8c. Three cutoff distances h_1, h_2, h_3 are introduced along three axis directions at the local coordinate system. Only if the ith integration point is within these cutoff distances, its weight function is calculated by Eq. (2.15). Obviously, it is efficient to numerically calculate the weight function. However, this method is valid based on the assumption that dislocation AB and A′B′ can be regarded as a 'dislocation pole'. Thus, at each time increment, the slip distance of each dislocation segment d_{slip} should be much smaller compared with its length.

2.2.1.2 Novel Regularization Method

To combine the advantages of previous regularization methods, a novel regularization method is proposed as schematically shown in Fig. 2.9. Inspired by Lemarchand et al.'s method [36], the regularization region is also considered as a slab with thickness equal to h, but the plastic strain is not localized according to the intersection volume. Similar to Liu et al.'s method, if the centroid of ith elementary volume is within the slab, or if the elementary volume is passed through by the swept area, its localized plastic strain $\Delta\gamma^{(i)}$ is given by a weight function $m^{(i)}$,

$$\Delta\gamma^{(i)} = \frac{m^{(i)}}{\sum_{i=1}^{n} m^{(i)}} \cdot \Delta\gamma^{\text{int}}, \quad m^{(i)} = \frac{S_{\text{swept}}^{(k)}}{S_{\text{all}}^{(k)}} \int_{V^i} \frac{1}{\pi} \frac{a}{d^{(i)2} + a^2} dV, \quad \text{if } d^{(i)} < \frac{h}{2} \tag{2.16}$$

where $d^{(i)}$ is the distance from the centroid of ith elementary volume to the slip plane. Compared with Liu et al.'s method, a coefficient $\frac{S_{\text{swept}}^{(k)}}{S_{\text{all}}^{(k)}}$ is introduced to characterize the slip extent, so dislocation AB and A′B′ do not have to meet the assumption of 'dislocation pole' and there is no constraint on the slip distance for each time increment. Specifically, the slab region is further divided into several subregions by element mesh as shown in Fig. 2.9. For the subregion corresponding to the kth swept elementary volume, $S_{\text{swept}}^{(k)}$ represents the swept area, and $S_{\text{all}}^{(k)}$ is the total possible swept area. For example, for blue subregion in Fig. 2.9b, the swept elementary volume is labeled as '3', $S_{\text{swept}}^{(k)}$ and $S_{\text{all}}^{(k)}$ are the area of CDOP and MNOP, respectively. MNFE is the cross section of the slab. If one dislocation line sweeps multiple elementary volumes in one time increment, this method still

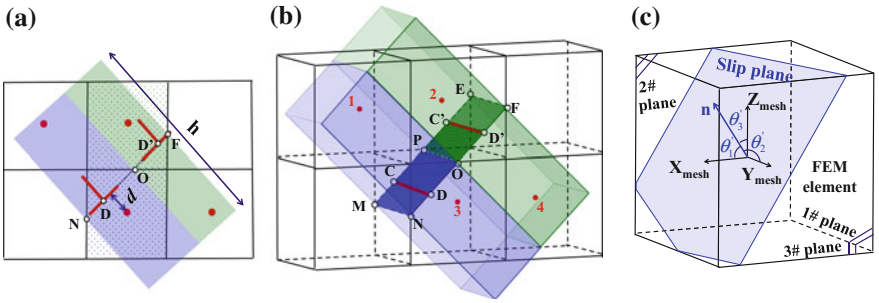

Fig. 2.9 **a–b** Schematic showing the new regularization method, from a view along dislocation line direction and 3D view, respectively. The *solid circle dot* represents the centroid of the concerned integration point volume. **c** Schematic definition of $\mathbf{X}_{\text{mesh}}$, $\mathbf{Y}_{\text{mesh}}$ and $\mathbf{Z}_{\text{mesh}}$, which are normal directions of the 1#, 2# and 3# FEM element planes, respectively. θ'_1, θ'_2, and θ'_3 are their angles with the normal direction of slip plane **n**, respectively. Reprinted from Ref. [41], Copyright 2015, with permission from Elsevier

exhibits high efficiency, because $\frac{S_{\text{swept}}^{(k)}}{S_{\text{all}}^{(k)}} = 1$ for most subregions and it is only required to calculate $\frac{S_{\text{swept}}^{(k)}}{S_{\text{all}}^{(k)}}$ for subregions near the boundary of the swept area.

In addition, all these regularization methods involves parameters (such as h), which are found to depend on the type of FEM element and the slip system information [36]. For example, for dislocation with slip plane parallel to one of the FEM mesh planes, it is found that good results can be obtained when the plastic strain is localized only to the swept elementary volumes. Thus, the regularization parameter h^{parallel} is set to $L/2$ for quadratic hexahedron element with 20 nodes and 8 Gauss points, where L is the element size. However, for tilted dislocation, the regularization region must be enlarged to assure the continuity of the eigenstrain from element to element. Till now, there is no quantitative suggestion about the chosen of regularization parameter. Our study shows that for arbitrary tilted dislocation, good results can be obtained if a slip plane dependent parameter h is determined as follows,

$$\begin{gathered} h = k_{\text{tilt}} h^{\text{parallel}}, \quad k_{\text{tilt}} = 1 + \sin 2\theta_1 + \sin 2\theta_2 + \sin 2\theta_3, \\ \theta_1' = \arccos\left(\frac{\mathbf{n} \cdot \mathbf{X}_{\text{mesh}}}{\|\mathbf{n}\| \cdot \|\mathbf{X}_{\text{mesh}}\|}\right), \quad \theta_2' = \arccos\left(\frac{\mathbf{n} \cdot \mathbf{Y}_{\text{mesh}}}{\|\mathbf{n}\| \cdot \|\mathbf{Y}_{\text{mesh}}\|}\right), \quad \theta_3' = \arccos\left(\frac{\mathbf{n} \cdot \mathbf{Z}_{\text{mesh}}}{\|\mathbf{n}\| \cdot \|\mathbf{Z}_{\text{mesh}}\|}\right) \\ \theta_1 = \min(\theta_1', \pi - \theta_1'), \quad \theta_2 = \min(\theta_2', \pi - \theta_2'), \quad \theta_3 = \min(\theta_3', \pi - \theta_3') \end{gathered} \tag{2.17}$$

where $\mathbf{n}$ is the normal vectors of slip plane, $\mathbf{X}_{\text{mesh}}$, $\mathbf{Y}_{\text{mesh}}$ and $\mathbf{Z}_{\text{mesh}}$ represent the normal directions of the FEM element planes as shown in Fig. 2.9c, and the angles with $\mathbf{n}$ are θ_1', θ_2', and θ_3', respectively. k_{tilt} is correction coefficient for regularization parameter h.

A simple numerical test is carried out to validate the effectiveness of the new regularization method for tilted dislocation lines. Considering a cubic crystal with side length 40 μm, an edge dislocation along [100] direction sweeps to the middle of the crystal along (010) slip plane, its burgers vector is along [001] direction. We restrict our study to isotropic elastic solid with shear modulus μ = 51 GPa and Poisson's ratio ν = 0.37 in most of the following simulations, unless specified otherwise. As suggested by Lemarchand et al. [36], a quadratic hexahedron element with 20 nodes and 8 Gauss points (C3D20R) is used in all of the present calculations. The element size is set to 850 nm. The results with $h = h^{\text{parallel}}$ and $h = k_{\text{tilt}} h^{\text{parallel}}$ are presented in Fig. 2.10a–c, d–f, respectively. It can be seen that when the regularization region is small, there will be numerical noise for the tilted dislocation. However, the stress filed can be reasonably captured by enlarging the regularization region controlled by slip plane dependent parameter.

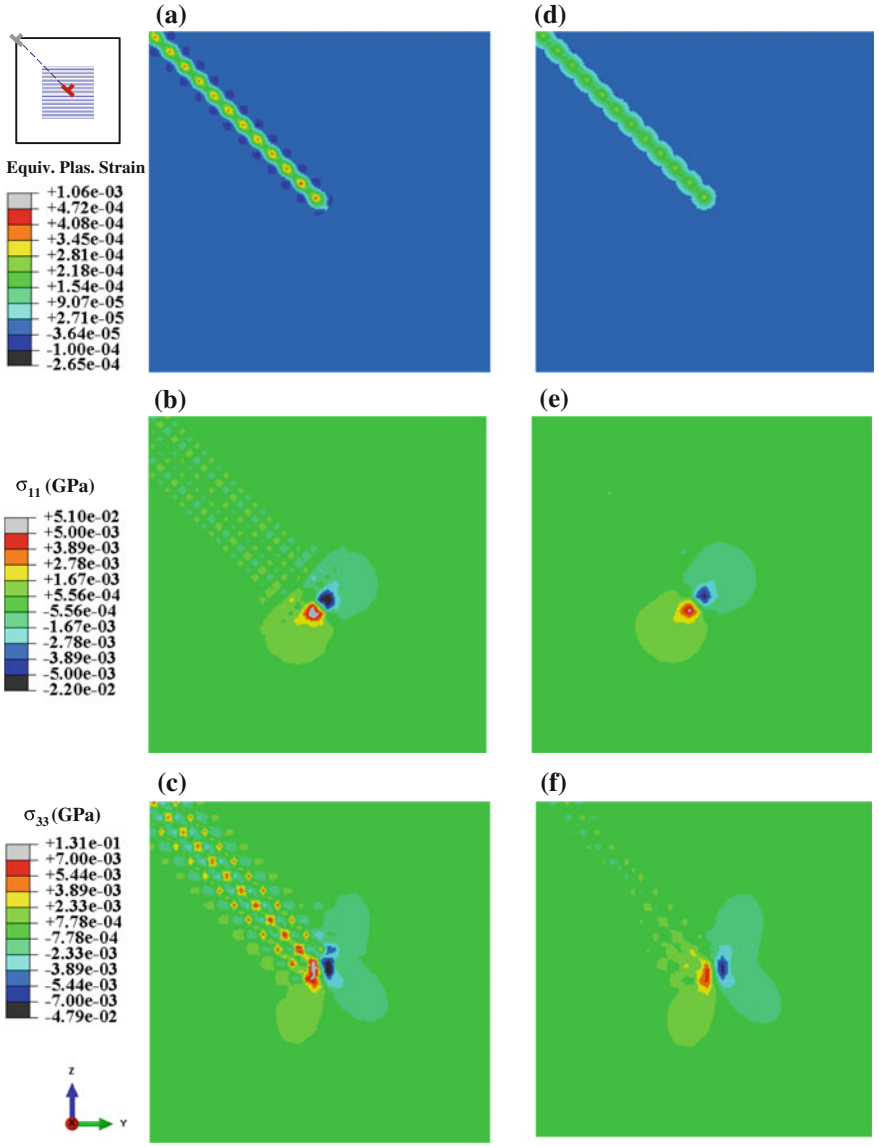

Fig. 2.10 For tilted dislocation, the distribution of equivalent plastic strain and stress field in the shadow region in (**a**). They are calculated using new regularization method with **a**–**c** $h = h^{\text{parallel}}$; **d**–**f** $h = k_{\text{tilt}} h^{\text{parallel}}$. Reprinted from Ref. [41], Copyright 2015, with permission from Elsevier

2.2.1.3 Stress Field Calculation of Prismatic Loop

The accuracy of new regularization method is further compared with the other methods using a numerical test. Since the dislocations in DCM are represented by the plastic strains caused by their slips, a reasonable regularization method should be able to well introduce the self-stress field of dislocation lines according to the localized strains.

Considering a cubic crystal with dimension 2250 × 2000 × 2250 nm^3, there is a square prismatic dislocation loop, which lies in (010) slip plane and has four ⟨100⟩ edge segments of length 250 nm, as illustrated in Fig. 2.11a. The Burgers vector is along [010] direction and has magnitude of 0.25 nm. Supposing that this dislocation loop is obtained by the growth of a very small loop, the plastic strain inside and around the dislocation loop is non-zero and can be localized to the material point by four kinds of regularization methods described in Sects. 2.2.1.1

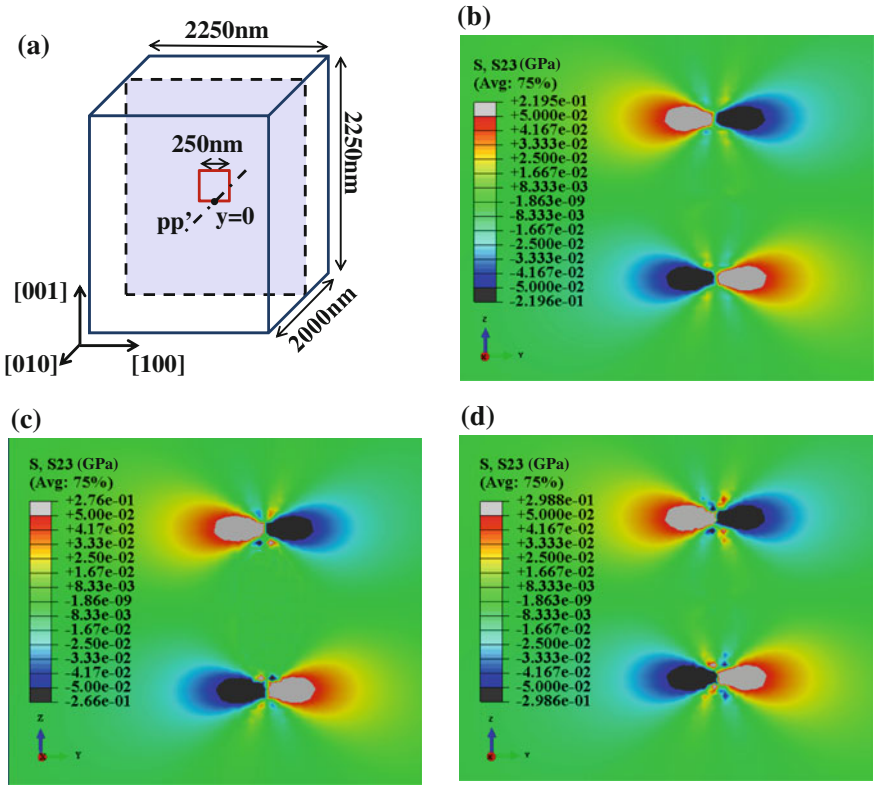

Fig. 2.11 **a** Geometrical description of the validation test, square prismatic dislocation loop in the dashed slip plane; **b–d** For element size L = 16 nm, distribution of shear stress σ_{23} caused by the prismatic loop using Lemarchand et al.'s method, Liu et al.'s method and new regularization method, respectively. Reprinted from Ref. [41], Copyright 2015, with permission from Elsevier

and 2.2.1.2. The regularization parameter h in Lemarchand et al.'s method and Vattré et al.'s method is taken as $3L/2$ [36]. The cutoff parameters in Liu et al.'s method is $h_1 = h_2 = h_3 = 2L/3$.

Different element sizes L are used in the calculation. The shear stress fields σ_{23} for $L = 16$ nm obtained by different regularization methods are given in Fig. 2.11b–d. The results for the Vattré et al.'s method can be obtained from reference [37] and are not shown here. The upper and lower bound of the stress value in Fig. 2.11b–d in this paper are set to the same as Fig. 10b in reference [37]. It can be noticed that a very similar stress distribution is obtained for different methods.

The stress variation along the dot dash line in Fig. 2.11a is further compared with the analytical solution when the element size L is set to 16 and 32 nm, respectively, as given in Fig. 2.12. It can be seen from Fig. 2.12a, b that different regularization methods display comparable accuracy. The singularity of stress near the dislocation core region is smeared out by all these regularization methods. This is very similar to the results derived by the non-singular continuum theory of dislocations proposed by Cai et al. [48]. To facilitate discussion, this region is

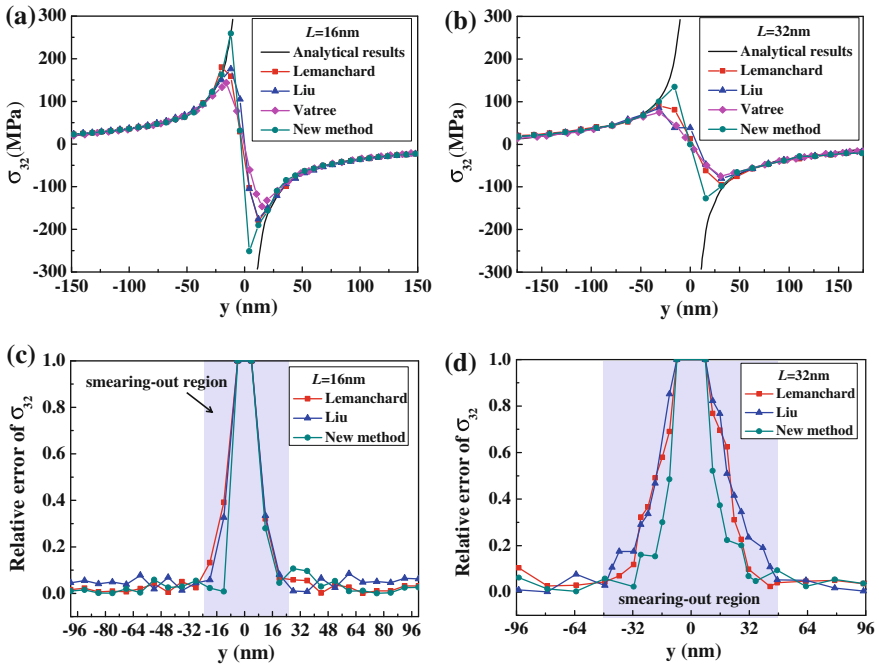

Fig. 2.12 **a–b** Stress component σ_{32} due to the prismatic loop by different regularization methods when element size L is 16 and 32 nm, respectively. The results for the method proposed by Vattré et al. are from Ref. [37] and the element sizes in (**a**) and (**b**) are 15 nm × 15.625 nm × 16.25 nm, 30 nm × 31.25 nm × 32.5 nm, respectively. **c–d** Relative errors of σ_{32} when element sizes are 16 and 32 nm, respectively. Reprinted from Ref. [41], Copyright 2015, with permission from Elsevier

denoted as 'smearing-out region' as labeled in Fig. 2.12c, d and the other region is denoted as 'long-range region'. The short-range interaction in the smearing-out region is required to be modified, such as using analytical solutions for dislocation interactions. By comparing Fig. 2.12c, d it can be found that increasing the element size does not strongly influence the precision in the long-range region, but enlarges the smearing-out region. Besides, the results suggest that the smearing-out region corresponds to the region where the distance to dislocation core is smaller than a critical value $r_{\text{smearing-out}}$. Quantitatively speaking, for the methods of Lemarchand et al. and Vattré et al., $r_{\text{smearing-out}}$ is 1.5 times the FEM element size L, which is exactly equal to the regularization parameter h [37]. For the method of Liu et al., $r_{\text{smearing-out}}$ is about twice the cutoff distance. For new regularization method, $r_{\text{smearing-out}}$ is equal to FEM element size L. In the long-range region, all the calculation results are in good agreement with analytical result, the relative error is less than 10 % (see Fig. 2.12 and Ref. [37]). Moreover, Fig. 2.12c, d illustrate that the precision for the new regularization method is even better than Lemarchand et al.'s method and Liu et al.'s method. Therefore, the new regularization method not only displays advantages as stated in Sect. 2.2.1.2, but also has good accuracy. With this in mind, DCM with new regularization method is mostly used in the following studies.

2.2.2 *Image Force Calculation*

The image force acting on dislocations near free surface is especially important at submicron scales because of the large specific surface area. Generally, it is always believed that DCM cannot accurately capture the image force, or at least, it is not comparable with SPM in this aspect. However, there is still no detailed analysis about how DCM can be improved to accurately capture the image force. In this section two corrections are proposed to improve the accuracy of image force calculation by DCM.

2.2.2.1 Stress Interpolation

In DCM, the image force is lumped into the total stress field calculated by FEM, and is passed to DDD according to stress-transfer procedure (see Fig. 2.5b). Specifically, the image force is calculated according to the difference of stress fields for two DCM models. One directly considers free surface, and the other calculates the total stress field in infinite body by applying the surface traction $\tilde{\mathbf{T}} = \boldsymbol{\sigma}^{\infty} \cdot \mathbf{n}_s$, where $\boldsymbol{\sigma}^{\infty}$ is analytical stress field of dislocations in an infinite media and $\mathbf{n}_s$ is the normal direction of surface. In the previous studies, the stress acting on each dislocation segment is usually taken to be equal to the stress at the integration point of FEM element where the midpoint of dislocation segment locates [11]. Since the

image force is strongly sensitive to the distance between the dislocation line and free surface, this kind of stress-transfer hardly gives good results when the dislocation segment does not exactly pass through the integration point. This can be demonstrated by a simple example below.

Considering a cubic crystal with side length 40 μm as shown in Fig. 2.13a, an edge dislocation along [100] locates at a distance Z below the [001] free surface, its burgers vector is along [001] direction. The image force induced by the top surface is calculated for different values of Z using DCM with new regularization method. The FEM element size L is set to 0.85 μm. The lines with triangle points in Fig. 2.13b are the results when image force on the dislocation segment is calculated using the stress at the nearest integration point. The results show rather large deviation from the analytical solution when the dislocation lines do not exactly pass through the integration points.

It is clear that a reasonable interpolation treatment of the stress field must be introduced to well capture the image force. Here, we propose that the stress σ at the considered dislocation segment is interpolated from the stress at the neighboring integration points,

$$\sigma = \begin{cases} \sigma^{(i)}, & \text{if} \quad d^{(i)}_{\text{seg-int}} = \min(d^{(1)}_{\text{seg-int}}, d^{(2)}_{\text{seg-int}}, \ldots) < r_{\text{infsmall}} \\ \dfrac{\sum_i \sigma^{(i)}/d^{(i)}_{\text{seg-int}}}{\sum_i 1/d^{(i)}_{\text{seg-int}}}, & \text{if} \quad r_{\text{infsmall}} < d^{(i)}_{\text{seg-int}} < r_{\text{cut}} \end{cases} \tag{2.18}$$

where $\sigma^{(i)}$ is the stress at the ith integration point, $d^{(i)}_{\text{seg-int}}$ is the distance between the midpoint of dislocation segment and the ith integration point as shown in Fig. 2.14. If the minimum distance between the midpoint of dislocation segment and the neighboring integration points is smaller than a critical value r_{infsmall}, it means that

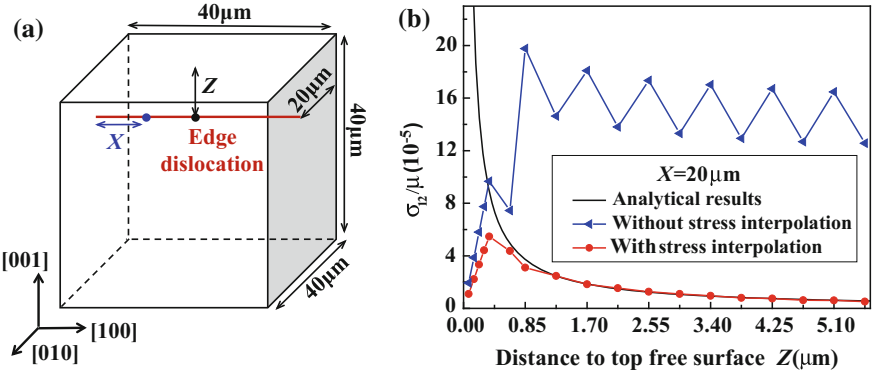

Fig. 2.13 **a** Description of the validation test; **b** comparison between the results calculated by DCM using new regularization method with and without stress interpolation. Reprinted from Ref. [41], Copyright 2015, with permission from Elsevier

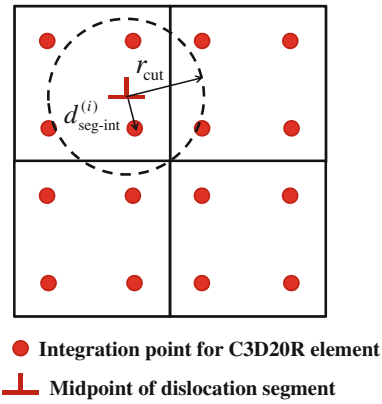

Fig. 2.14 Schematic definition of the variables used for stress interpolation. Reprinted from Ref. [41], Copyright 2015, with permission from Elsevier

the dislocation segment almost passes through an integration point, and no stress interpolation is required. Otherwise, the stress interpolation is carried out. It is found that good results can be obtained when the cutoff radius for interpolation region r_{cut} is set to $0.45L$, where L is the element size.

The image force calculation with stress interpolation is further carried out for the above validation test. The results in Fig. 2.13b highlight the great improvement after using stress interpolation modification. Next, the simulations using the other regularization methods but with stress interpolation are also carried out for the validation test in Fig. 2.13a. The calculated image forces are given in Fig. 2.15a. It can be found that the results using regularization methods proposed by Liu et al. and Lemarchand et al. are acceptable when the distance Z is larger than L and $5L/4$, respectively. While the new regularization method and Vattré et al.'s method can exhibit good accuracy until Z is smaller than $3L/4$. This further illustrates the advantage of new regularization method.

The other interesting issue is to compare the image force captured by DCM and SPM. Three typical cases are considered here: the first one is the same as the subsurface dislocation shown in Fig. 2.13a; the second one is calculating the image force along the dislocation line which perpendicularly intersects the free surface as shown in the inset of Fig. 2.15b; the third one is calculating the image force along a dislocation loop as shown in Fig. 2.15c. Under these cases, the element size is taken to be 0.85 μm both in DCM and SPM.

The simulation results of image force on the subsurface dislocation and intersection dislocation are presented in Fig. 2.15a, b respectively. For these two cases, the comparison with analytical results illustrates that under both cases, DCM using new regularization method can well calculate the image force for the distance to free surface larger than $3L/4$, which is similar to that of SPM. For the third case, since there are no analytical results for comparison, the calculated image force by DCM and SPM along the dislocation loop is compared with the results obtained by SPM with finer element sizes (L = 600 nm, which is limited by the large number of elements a single processor can handle). The results are in a good agreement as

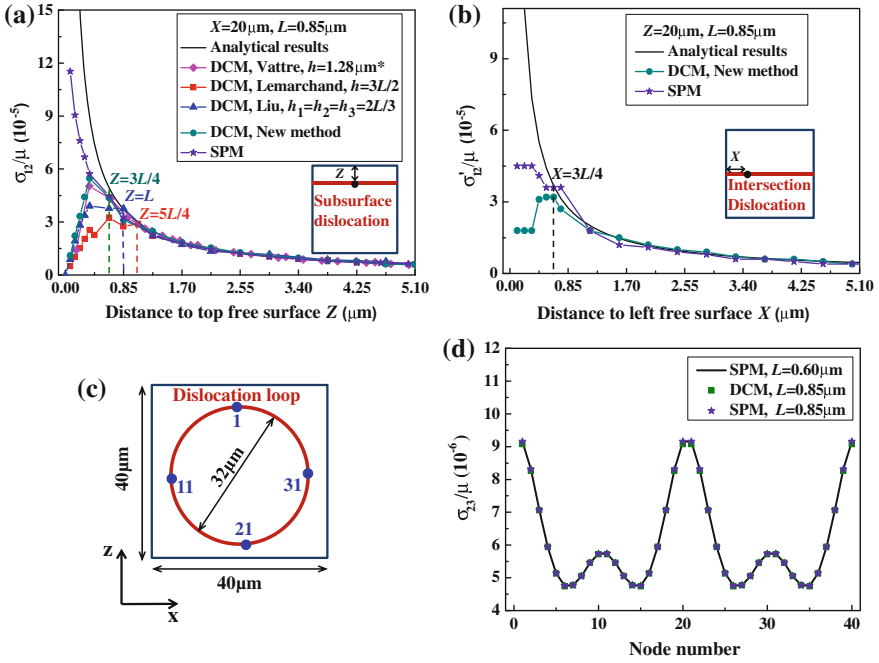

Fig. 2.15 **a** The image force induced by top free surface calculated by DCM using different regularization methods and SPM; The results marked by '*asterisk*' is obtained from Ref. [37]. **b** Image force σ'_{12} induced by left free surface when the dislocation segments intersect left free surface. The definitions of distances Z and X are given in the corresponding inset and Fig. 2.13a. **c** Description of the validation test for dislocation loop. Four dislocation node numbers are labeled. **d** Comparison between the results of image force calculated by DCM and SPM. Reprinted from Ref. [41], Copyright 2015, with permission from Elsevier

shown in Fig. 2.15d. Obviously, the widely used method of introducing SPM to DCM with the aim of correcting image force is inappropriate and will double-count the image force effect.

Moreover, it can be found from Fig. 2.15a, b that the image force very close to the free surface cannot be captured by either DCM or SPM because it is difficult for the linear or quadratic shape functions of standard FEM to describe the strong nonlinear variation of the field variables close to the surface. Therefore, when the dislocation line enters the near-surface region, a reasonable correction of image force must be introduced.

2.2.2.2 Hybrid DCM Method

The most straightforward method to correct image force in DCM is identifying the outermost two layer elements as a sub-domain, and then refining the elements in

this sub-domain. However, this undoubtedly increases the computation time, especially for three-dimension problem. Tang et al. [49] proposed a hybrid SPM method, in which the singular part of the image stress is obtained by analytical solution and the non-singular part is calculated by SPM. Here we extend this hybrid scheme to improve the ability of DCM in capturing image force. However, special attention must be paid since the image force is lumped into the total stress field in DCM. Under complex loading condition, it is difficult to isolate the image force calculated by DCM. Therefore, the stress field in infinite body must be taken into account in the decomposition and superposition framework, as schematically shown in Fig. 2.16. The singular image stress on AA′ $\sigma^{\text{ana\_imag}}$ in the elastic half-space is calculated according to Yoffe solution [50]. The difference in dislocation configuration between Fig. 2.16a, b is shown in Fig. 2.16c, whose total stress field $\boldsymbol{\sigma}^{\text{corr\_img}} + \boldsymbol{\sigma}^{\infty}_{A'B} + \boldsymbol{\sigma}^{\infty}_{BD}$ can be calculated by DCM. Then, the stress field caused by semi-infinite dislocation AA′ $\boldsymbol{\sigma}^{\infty}_{AA'}$ should be added as shown in Fig. 2.16d according to Li solution [51]. This part on the one hand removes the stress field caused by dislocation A′B, and on the other hand adds the stress field caused by dislocation AB, $\boldsymbol{\sigma}^{\infty}_{AA'} = \boldsymbol{\sigma}^{\infty}_{AB} - \boldsymbol{\sigma}^{\infty}_{A'B}$. Accordingly, the total stress field in half space can be expressed as $\boldsymbol{\sigma}^{\text{tot}} = \boldsymbol{\sigma}^{\text{ana\_img}} + (\boldsymbol{\sigma}^{\text{corr\_img}} + \boldsymbol{\sigma}^{\infty}_{A'B} + \boldsymbol{\sigma}^{\infty}_{BD}) + (\boldsymbol{\sigma}^{\infty}_{AB} - \boldsymbol{\sigma}^{\infty}_{A'B})$. According to the work of Tang et al. [49], this hybrid method can also be used to solve the problem with multiple free surfaces.

To show its effectiveness, the image force on a curve dislocation line in the cubic crystal is calculated (see the inset of Fig. 2.17). It locates at (010) slip plane, and its burgers vector is along [001] direction. The image force induced by the left free surface is calculated for different values of X using DCM and hybrid DCM. The results in Fig. 2.17 show that hybrid DCM method can well capture the singular image force near the free surface.

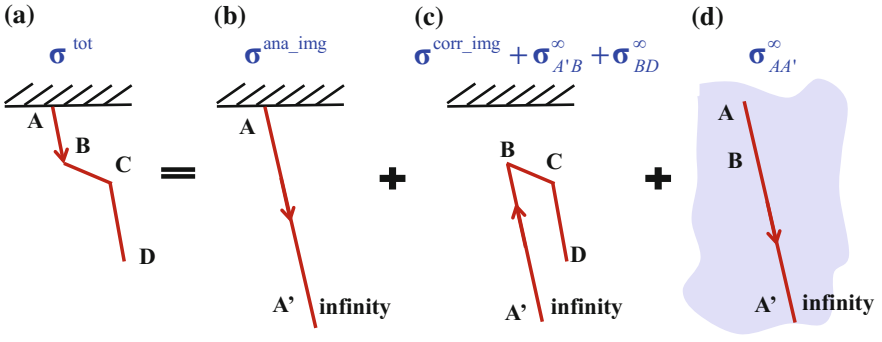

Fig. 2.16 Schematically illustration of the hybrid DCM method when calculating image force on an arbitrary curved dislocation line in a half-space with only one free surface. Reprinted from Ref. [41], Copyright 2015, with permission from Elsevier

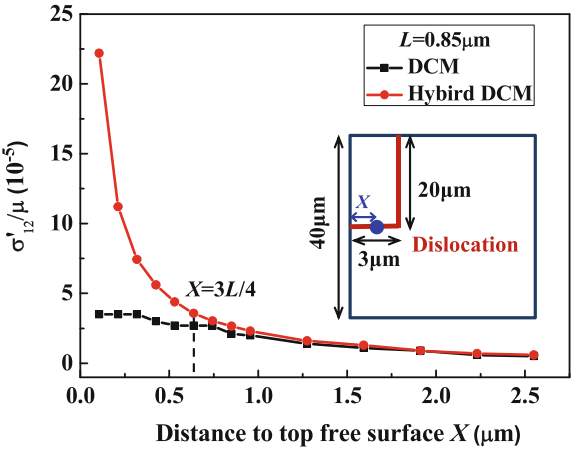

Fig. 2.17 Image force σ'_{12} induced by the left free surface. The *Inset* shows the dislocation configuration. Reprinted from Ref. [41], Copyright 2015, with permission from Elsevier

2.2.3 *Finite Deformation*

Capturing the deformed configuration by DCM is another important issue to understand the material deformation and failure process at submicron scales [45]. In this section, a new algorithm is developed to calculate deformed configuration in DCM, and two validation tests are carried out to quantitatively show how DCM can be used to capture the strong localized deformation.

2.2.3.1 Deformation Field Transfer and Surface Dislocation Treatment

In order to reproduce the deformed configuration accurately, the DDD computation cells must deform in accordance with the FEM cells [11]. Thus, the position of dislocation segments is updated according to its own slip $\mathbf{u}^{I}_{\text{slip}}$ and the deformation induced displacement $\mathbf{u}^{(I)}_{\text{DDD}}$,

$$\mathbf{u}^{(I)} = \mathbf{u}^{(I)}_{\text{slip}} + \mathbf{u}^{(I)}_{\text{DDD}} \tag{2.19}$$

where the subscript "(I)" denotes the node number of dislocation segment in DDD. $\mathbf{u}^{(I)}_{\text{slip}}$ is directly calculated by DDD model,

$$\mathbf{u}^{(I)}_{\text{slip}} = \mathbf{v}^{(I)}_{\text{slip}} \Delta t \tag{2.20}$$

where $\mathbf{v}^{(I)}_{\text{slip}}$ is the velocity of dislocation node and can be calculated according to its kinetic equation,

$$\mathbf{M_d}\dot{\mathbf{v}}_{\text{slip}}^{(I)} + \mathbf{B}\mathbf{v}_{\text{slip}}^{(I)} = \mathbf{f}^{(I)} \tag{2.21}$$

where $\mathbf{M_d}$ and $\mathbf{B}$ are the corresponding effective mass matrix and the drag coefficient matrix, respectively. The first inertia term on the left side can be ignored when the dislocation motion is in the over-damped regime. The force vector $\mathbf{f}^{(I)}$ of segment I includes the Peach-Koehler force by applied stress and other defects, line tension, as well as image force.

Deformation induced displacement $\mathbf{u}_{\text{DDD}}^{I}$ is obtained by FEM calculation and passed to DDD model. Considering the simplest case, if the dislocation does not move, the displacement at dislocation segment node I is just equal to $\mathbf{u}_{\text{DDD}}^{I}$. Specifically, $\mathbf{u}_{\text{DDD}}^{I}$ is obtained by interpolating the displacement of FEM nodes around the dislocation segment node "I". Here, an interpolation scheme similar to Eq. (2.18) is used,

$$\mathbf{u}_{\text{DDD}}^{(I)} = \begin{cases} \mathbf{u}_{\text{DDD}}^{(k)}, & \text{if } d_{\text{seg-node}}^{(k)} = \min(d_{\text{seg-node}}^{(1)}, d_{\text{seg-node}}^{(2)}, \ldots) < r_{\text{infsmall}} \\ \dfrac{\sum_i \mathbf{u}_{\text{DDD}}^{(k)} / d_{\text{seg-node}}^{(k)}}{\sum_i 1/d_{\text{seg-node}}^{(k)}}, & \text{if } r_{\text{infsmall}} < d_{\text{seg-node}}^{(k)} < r_{\text{cut}} \end{cases} \tag{2.22}$$

where the superscript "(k)" denotes the variables associated with the kth FEM node. $d_{\text{seg-node}}^{(k)}$ is the distance between the midpoint of the dislocation segment and the kth FEM node. If the minimum distance between the midpoint of dislocation segment and FEM nodes is smaller than an infinitely small value r_{infsmall}, no displacement interpolation is required. As shown in Fig. 2.14, r_{cut} is also the cutoff radius for interpolation region.

At the same time, a special treatment must be used to treat the surface annihilation and guarantee that the surface-piercing dislocation segments remain surface-piercing instead of terminating in the interior of the sample. To achieve this, in the FEM model we define the surface element as a separate part which is used to conveniently transfer information with the boundary of DDD cell. This makes it very easy to update the external geometry of the DDD cell and deal with the surface annihilation.

Specifically, during each step, if dislocations slip out of the crystal, the outside part is deleted to deal with the surface annihilation. In addition, the intersection nodes between the surface segments and free surface are labeled as surface nodes. If the dislocation line intersects a convex surface, the velocity of the surface node $\mathbf{v}_{\text{surfnode}}$ is projected to match the local curvature of free surface and fulfill the constriction of the slip plane, as described below [52],

$$\begin{aligned} \mathbf{n}_{\text{surfnode}} &= \frac{\mathbf{n} \times \mathbf{n}_{\text{s}}}{\|\mathbf{n} \times \mathbf{n}_{\text{s}}\|} \\ \mathbf{v}_{\text{surfnode}} &= \left(\mathbf{v}_{\text{slip}} \cdot \mathbf{n}_{\text{surfnode}}\right)\mathbf{n}_{\text{surfnode}} \end{aligned} \tag{2.23}$$

where $\mathbf{n}_{\text{surfnode}}$ is a unit vector indicating the intersection between the surface and slip plane, $\mathbf{n}$ and $\mathbf{n}_s$ are the normal vectors of slip plane and local free surface, respectively. The introduction of surface element part in FEM model makes the calculation of $\mathbf{n}_s$ very easy.

On the other hand, if the dislocation line slips across a concave surface, such as induced by an evident slip step, the velocity projection and the displacement correction by FEM model are not enough. It is required to check whether the surface node remains on the surface after deformation. If the surface dislocations are found to terminate in the bulk, the surface dislocation lines should be extended to intersect with free surface.

2.2.3.2 Slip System Rotation

The FEM model can conveniently consider the lattice rotation effect. To incorporate the lattice rotation effect in 3D DDD code, the dislocation slip systems are directly updated according to large-strain kinematics in crystal plasticity theory [53],

$$\begin{aligned} \mathbf{b}_{(t)} &= \mathbf{F}^{\mathrm{e}} \cdot \mathbf{b}_{(t_0)} \\ \mathbf{n}_{(t)} &= \mathbf{n}_{(t_0)} \cdot \mathbf{F}^{\mathrm{e}-1} \end{aligned} \tag{2.24}$$

where $\mathbf{b}$ is burgers vector, $\mathbf{n}$ is the normal vector of slip plane, the subscripts (t) and (t_0) refer to the values of the variables at time t and $t_0 = 0$, respectively. $\mathbf{F}^{\mathrm{e}}$ represents the elastic stretching and rotation of the crystal lattice, which can be determined by the multiplicative decomposition of deformation gradient $\mathbf{F}$,

$$\begin{aligned} \mathbf{F} &= \mathbf{F}^{\mathrm{e}} \cdot \mathbf{F}^{\mathrm{p}} \\ \mathbf{L}^{\mathrm{p}} &= \dot{\mathbf{F}}^{\mathrm{p}} \cdot \mathbf{F}^{\mathrm{p}-1} = \dot{\gamma} \left(\frac{\mathbf{b}}{\|\mathbf{b}\|} \otimes \frac{\mathbf{n}}{\|\mathbf{n}\|} \right) \end{aligned} \tag{2.25}$$

where $\mathbf{F}^{\mathrm{p}}$ is the plastic part of $\mathbf{F}$ induced by the plastic slip, $\mathbf{L}^{\mathrm{p}}$ is the plastic part of velocity gradient, and $\dot{\gamma}$ is the plastic shear strain rate calculated by the regularization methods. By taking the derivative of Eq. (2.24), the following relation can be obtained,

$$\begin{aligned} \dot{\mathbf{b}}_{(t)} &= \dot{\mathbf{F}}^{\mathrm{e}} \cdot \mathbf{F}^{\mathrm{e}-1} \cdot \mathbf{b}_{(t)} \\ \dot{\mathbf{n}}_{(t)} &= -\mathbf{n}_{(t)} \cdot \dot{\mathbf{F}}^{\mathrm{e}} \cdot \mathbf{F}^{\mathrm{e}-1} \end{aligned} \tag{2.26}$$

where a superposed dot means time derivative. Then, combining Eq. (2.25) and Eq. (2.26), the slip system can be updated by the following implicit time-integration,

$$\begin{aligned}
\mathbf{b}_{(t+\Delta t)} &= (\mathbf{I}+\dot{\mathbf{F}}^{\mathrm{e}}\cdot\mathbf{F}^{\mathrm{e}-1}\Delta t)\cdot\mathbf{b}_{(t)}\\
\mathbf{n}_{(t+\Delta t)} &= \mathbf{n}_{(t)}\cdot(\mathbf{I}-\dot{\mathbf{F}}^{\mathrm{e}}\cdot\mathbf{F}^{\mathrm{e}-1}\Delta t)\\
\dot{\mathbf{F}}^{\mathrm{e}}\cdot\mathbf{F}^{\mathrm{e}-1} &= \dot{\mathbf{F}}\cdot\mathbf{F}^{-1}-\mathbf{F}\cdot\mathbf{F}^{\mathrm{p}-1}\cdot\dot{\mathbf{F}}^{\mathrm{p}}\cdot\mathbf{F}^{-1},\dot{\mathbf{F}}^{\mathrm{p}}=\mathbf{L}^{\mathrm{p}}\cdot\mathbf{F}^{\mathrm{p}},\\
\mathbf{F}^{\mathrm{p}}_{(t+\Delta t)} &= \mathbf{F}^{\mathrm{p}}_{(t)}+\dot{\mathbf{F}}^{\mathrm{p}}_{(t)}\Delta t=(\mathbf{I}+\mathbf{L}^{\mathrm{p}}\Delta t)\cdot\mathbf{F}^{\mathrm{p}}_{(t)}
\end{aligned} \tag{2.27}$$

where Δt is time increment, $\mathbf{I}$ is unit tensor. The result of $\dot{\mathbf{F}}^{\mathrm{e}}\cdot\mathbf{F}^{\mathrm{e}-1}$ is transferred from FEM model to DDD model, as shown in Fig. 2.5b. The corresponding interpolation scheme is similar to Eq. (2.18). At the same time, the deformation field transfer from FEM to DDD described in Sect. 2.2.3.1 can naturally consider the update of position and orientation for dislocation lines induced by lattice rotation.

Two validation tests are given below to show its effectiveness. The first one is schematically shown in Fig. 2.18a, b. An edge dislocation nucleates from the surface (labeled as A) and glides to the middle of the crystal (labeled as A′). At the same time, the crystal rotates 45° about the [100] axis. The FEM mesh size is 0.85 μm. If the rotation is not considered, the stress field cannot be accurately captured as shown in Fig. 2.18c. However, if it is considered according to Eq. (2.27), the calculated stress filed is reasonable as shown in Fig. 2.18d.

The second validation test is to investigate the evolution of a Frank-Read source in a bended beam with length 50 μm and cross section area 10 μm × 10 μm. This Frank-Read source is originally situated along [100] direction in (010) slip plane with burger vector [001]. The FEM element size is 2 μm. To clearly show the evolution of dislocation configuration and save computational time, the strain rate for bending is set to be so large that the dislocation configuration does not have enough time to reach a fully relaxed configuration during deformation. During each time increment of FEM model $\Delta t_{\mathrm{FEM}} = 1.6 \times 10^{-8}$ s^{-1}, the displacement increment ΔU_2 is 0.1 μm, and the DDD model runs 400 times with time increment $\Delta t_{\mathrm{DDD}} = 4\times10^{-11}$ s^{-1}. The simulation results are given in Fig. 2.19 when U_2 is

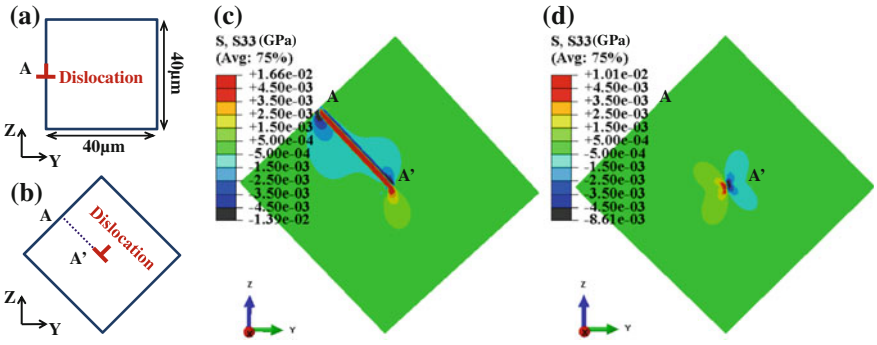

Fig. 2.18 **a–b** Sample geometry and dislocation position before and after deformation, respectively. **c–d** Stress field σ_{33} without and with slip system rotation treatment, respectively. Reprinted from Ref. [41], Copyright 2015, with permission from Elsevier

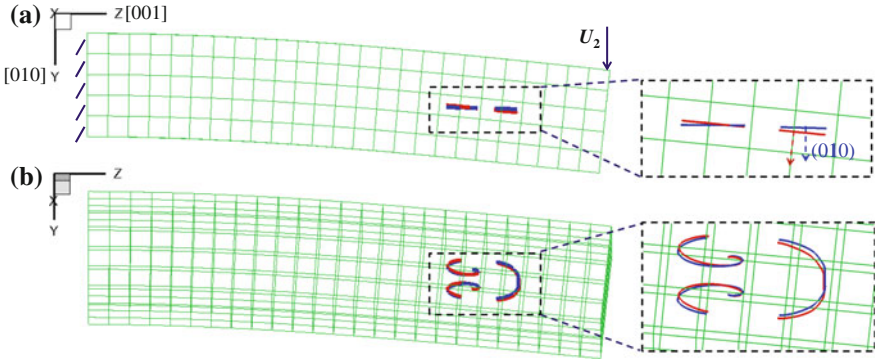

Fig. 2.19 An overlay of snapshots of dislocation configurations for bended beam without and with lattice rotation when $U_2 = 3.5$ μm, the *blue* and *red* dislocation lines correspond to the results without and with rotation, respectively. **a** and **b** are results from different views. Reprinted from Ref. [41], Copyright 2015, with permission from Elsevier

3.5 μm. Figure 2.19a shows that if the lattice rotation effect is ignored, the position of the dislocation can be updated, but the slip plane is kept as (010). However, if the lattice rotation effect is considered, the slip plane rotates precisely with the rotation of the neutral axis.

2.2.3.3 Reproduction of Slip Step

In the following, two validation tests are carried out to investigate the ability of improved DCM in capturing deformed configuration.

One validation case is an edge dislocation line sweeping a finite cubic sample, as described in Fig. 2.13a. The element size is 850 nm. The simulation results are given in Fig. 2.20. Here, the displacements are magnified by a factor of 5000 for better visualization. When this dislocation line sweeps half of the slip plane, only the left slip step can be observed (Fig. 2.20a); when this dislocation line sweeps the whole slip plane, one slip step with the magnitude of burger vector (0.25 nm) is generated as expected (Fig. 2.20b). This implies that the displacement field can be well reproduced by introducing the localized plastic strain from DDD to FEM.

In submicron crystals, it is widely accepted that the operation of single arm source is the dominated dislocation mechanism [6, 54]. Thus, the other validation case is chosen to be a single arm source sweeping a micropillar with diameter 1000 nm and height 2000 nm. This single arm source is placed on (111) slip plane with Burgers vector along $[10\bar{1}]$. It has one non-destructible pinning point at the central point of the micro-pillar. The element size of FEM model is 80 nm, which is found to permit fine resolutions with accurate result and convergence. The uniaxial compression loading is applied on the top of pillar with constant pressure 200 MPa. Since the resolved shear stress to active this single arm source is much less than that

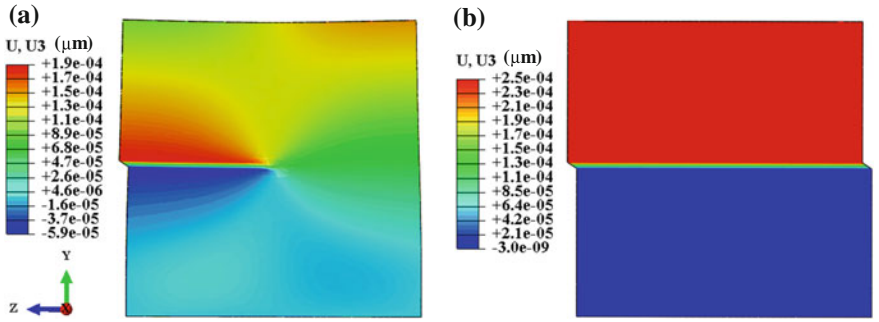

Fig. 2.20 Deformed configuration with displacement magnified by a factor of 5000 **a** when an edge dislocation line sweeps half of the sample; **b** when an edge dislocation line sweeps the whole sample. Reprinted from Ref. [41], Copyright 2015, with permission from Elsevier

generated by the external pressure, the single arm source can continuously operate, which leads to significant localized deformation (see Fig. 2.21a). Compared with the first validation case, this numerical test can be used to check whether the deformed shape can be well reproduced by DCM, when the FEM elements swept by the dislocation segments are irregular, the dislocation line is curved, and localized deformation happens.

According to Eq. (2.11), the plastic strain is determined by the sweep area of dislocation segments. Thus, the distribution of plastic strain is very sensitive to the dislocation configuration. Once the surface segments shrinks, the plastic strain value in near-surface region is small compared with the other regions. The simulation results in Fig. 2.21b show that the equivalent plastic strain is uniform even under the case of large deformation and irregular mesh.

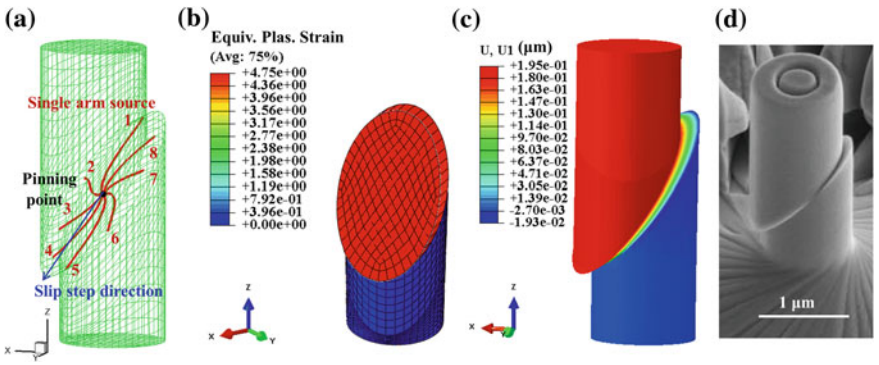

Fig. 2.21 When the single arm source sweeps a slip plane for 1000 times, **a** an overlay of snapshots showing the dislocation configuration and deformed shape; **b** distribution of equivalent plastic strain, which is observed on a cross-section along the (111) plane and **c** the displacement field U_1. Reprinted from Ref. [41], Copyright 2015, with permission from Elsevier; **d** SEM image showing the deformed configuration of 1 μm diameter micropillar [44]

Furthermore, the simulation results are quantitatively evaluated. When the slip plane is swept by a single arm source for n times, the slip distance along a slip step direction (see arrow in Fig. 2.21a) is $n\,|\mathbf{b}|$. For the considered case, the displacement along x direction U_1 should be equal to $n|\mathbf{b}|/\sqrt{2}$. Taking $n = 1000$ as an example, the value of U_1 should be 0.18 μm. It can be seen from Fig. 2.21c that the simulated displacement U_1 for the upper part of the sample is exactly close to this value. In addition, the deformed configuration is very similar to the experimental observations as shown in Fig. 2.21d [44]. Note that if there are dislocations existing in the upper part of the pillar shown in Fig. 2.21a, they will shift a displacement equal to U_1 along x direction according to Eq. (2.19).

2.2.4 Application in Heteroepitaxial Film

As an example, the modified DCM is applied to study the dislocation behavior in heteroepitaxial films, which has recently received a great deal of attention due to their wide applications in semiconductor and electron device industry. The thermoelastic analogical calculation is conducted to calculate the internal stress field induced by the lattice misfit between film and substrate. The dislocation behaviors and corresponding stress fields are analyzed for thin/thick substrates.

2.2.4.1 Thermoelastic Calculation to Determine Internal Stress Field

Considering the $Si_{1-x}Ge_x$/Si film-substrate structure, the lattice misfit strain is set to $\varepsilon_m = (a_{SiGe} - a_{si})/a_{si} = 0.0418x = 0.0055$ for $x = 0.13$ [55], where a_{SiGe} and a_{si} is the lattice constant of film and substrate, respectively. In previous studies, the initial stress field caused by misfit strain is usually imposed by analytical solutions through assuming that the film and substrate have the same material parameters [55]. In the present work, it is calculated by analogizing the lattice misfit as a thermal expansion process for two materials with different thermal expansion coefficients α. The thermal expansion coefficients of film α_f and substrate α_s, respectively, are set to,

$$\begin{aligned} \alpha_f &= \varepsilon_m \frac{d_s E_{Si}}{d_f E_{SiGe} + d_s E_{Si}} \\ \alpha_s &= -\varepsilon_m \frac{d_f E_{SiGe}}{d_f E_{SiGe} + d_s E_{Si}} \end{aligned} \tag{2.28}$$

Here, both $Si_{1-x}Ge_x$ film and Si substrate are assumed isotropic. $E_{si} = 130$ GPa is the elastic modulus of Si [56]. E_{Ge} is the elastic modulus of Ge and set to 102.5 GPa [57]. The elastic modulus of $Si_{1-x}Ge_x$ $E_{SiGe} = E_{si}\ (1 - x) + E_{Ge}x$, is approximated by a linear rule of mixtures. d_f is the thickness of film and set to

0.3 μm. d_s is the thickness of substrate and set to 0.6 and 3 μm to simulate very thin and very thick substrates, respectively. Besides, the side length of film and substrate is set to 20 μm. The out-of-plane displacement at the bottom surface of substrate is fixed to constraint the laterally bending. All the other surfaces are traction free. The stress field corresponds to the result when the temperature increases one unit value.

Firstly, the accuracy of this thermoelastic analogical method is verified. When the film is assumed to have the same elastic modulus as the substrate E_{si}, the analytical stress field is obtained,

$$\begin{aligned}\sigma_f &= -\frac{E_{si}}{1-\nu_{si}}\frac{d_s}{d_f+d_s}\varepsilon_m \\ \sigma_s &= \frac{E_{si}}{1-\nu_{si}}\frac{d_f}{d_f+d_s}\varepsilon_m\end{aligned} \tag{2.29}$$

where ν_{si} is the Poisson's ratio of Si and set to 0.28 [56]. When d_s is taken to be 0.6 μm, $\sigma_f = -0.662$ GPa, and $\sigma_s = 0.331$ GPa. The FEM mesh size is 0.06 μm in the thickness direction and 0.4 μm in the other two directions. The simulation results are presented in Fig. 2.22. It can be seen from Fig. 2.22a that except the region near the boundary, the stress field is consistent with the analytical result. Figure 2.22b further compares the stress value along the thickness (dotted line in Fig. 2.22a) obtained by simulation and Eq. (2.29). A good quantitative agreement is observed.

2.2.4.2 Influence of Substrate Thickness on Dislocation Behavior

By the thermoelastic analogical calculation, the internal stress field can be obtained when the film and substrate have different mechanical properties. Next the evolution of a Frank-Read source in this internal stress field is simulated by the improved DCM to clearly depict the dislocation behavior in heteroepitaxial film with different thicknesses of substrate.

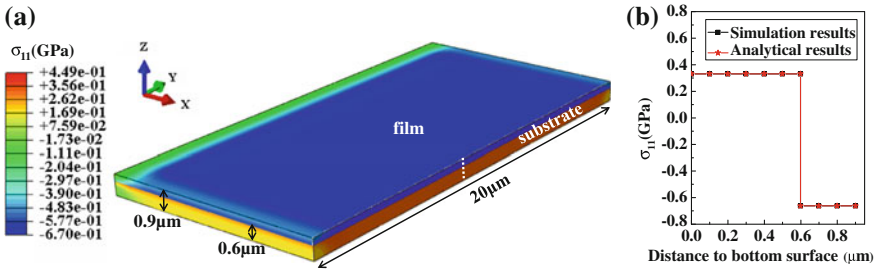

Fig. 2.22 **a** [100] Cross-sectional view showing the stress field σ_{11} for heteroepitaxial film and substrate, when the film and substrate are assumed to have the same elastic modulus. **b** Comparison of σ_{11} along the thickness [*dotted line* in (**a**)] for simulation and analytical results. Reprinted from Ref. [41], Copyright 2015, with permission from Elsevier

Supposing initially there is a Frank-Read source in (111) slip plane with burgers vector along $[\bar{1}01]$ in the middle of film, it naturally multiplies under the action of free surface and internal stress field, without any prior constraint on dislocation motion. The pinning points are indestructible and 200 nm apart. The image force caused by the free surface is modified by the hybrid method described in Sect. 2.2.2.

The calculated dislocation microstructure evolution for the cases of thin and thick substrate is shown by the black solid lines in Fig. 2.23a–e and e–j respectively. Under both cases, threading dislocations form when the bowing-out dislocation segments encounters free surface, while misfit dislocations form when they intersect with film-substrate interface. With the image force correction, the near-surface threading dislocation segments are almost perpendicular to free surface, which is consistent with previous phase field method studies [55]. Comparing Fig. 2.23d with Fig. 2.23i, the misfit dislocations behave differently for different substrate thicknesses. For very thick substrate, the misfit dislocations can penetrate into the substrate when two misfit dislocations form (see Fig. 2.23i–j), whereas for thin substrate, the penetration of misfit dislocation is not observed in Fig. 2.23e due to the higher compression stress in the substrate. Therefore, for the case of thin

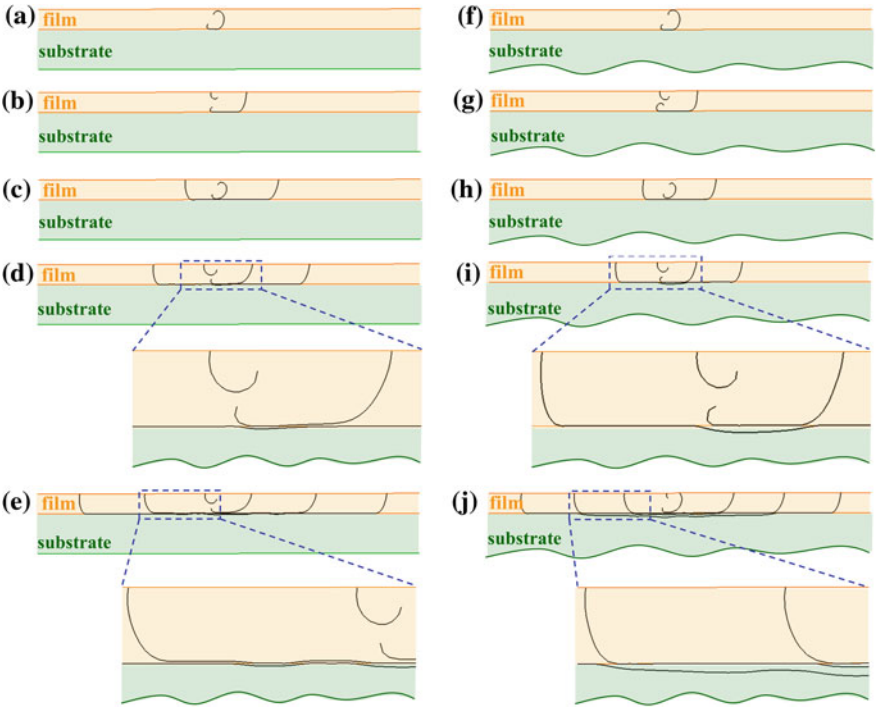

Fig. 2.23 **a–e** Dislocation evolution in film with thin substrate; **f–j** Dislocation evolution in film with thick substrate. The *black solid lines* represent the dislocation lines. Reprinted from Ref. [41], Copyright 2015, with permission from Elsevier

substrate, the back stress induced by the misfit dislocations is higher and will inhibit the operation of Frank-Read source. Even though the length of the longest misfit dislocation lines in Fig. 2.23e, j are almost equal, the cycles of Frank-Read source operation are different.

The stress fields without and with dislocations are compared in Fig. 2.24b, c for thin substrate, Fig. 2.25b, c for thick substrate, respectively, to illustrate the role of dislocation evolution on the strain relaxation. It can be noticed that for both thin and thick substrates, the Mises stress in the film decreases because the misfit strain is relaxed as the glide of dislocations. Comparing Fig. 2.24b with Fig. 2.24c, it can be found that the piling-up misfit dislocations at the interface lead to the increase of stress in the thin substrate. In contrast, as shown in Fig. 2.25b, c, there is no evident change of the stress in the substrate after multiple misfit dislocations form since they can penetrate towards thick substrate. The simulation implies that the crack nucleation and interface delamination are more likely to happen for thin substrate.

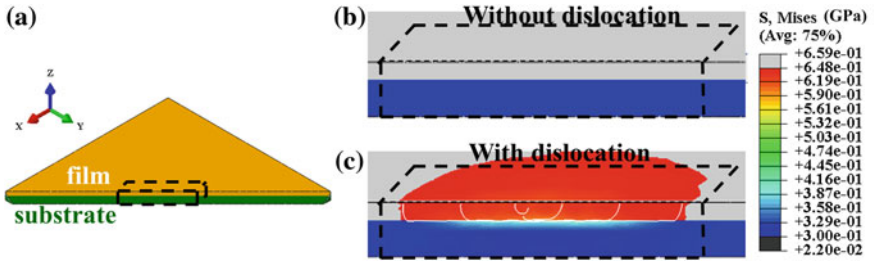

Fig. 2.24 (111) plane cross-sectional view showing the concerned region enclosed by dotted lines for film with thin substrate; **b–c** Mises stress field in the concerned region labeled in (**a**) before and after dislocation source operation, respectively. The *while solid lines* in (**c**) represent the dislocation lines, which corresponds to Fig. 2.23e. Reprinted from Ref. [41], Copyright 2015, with permission from Elsevier

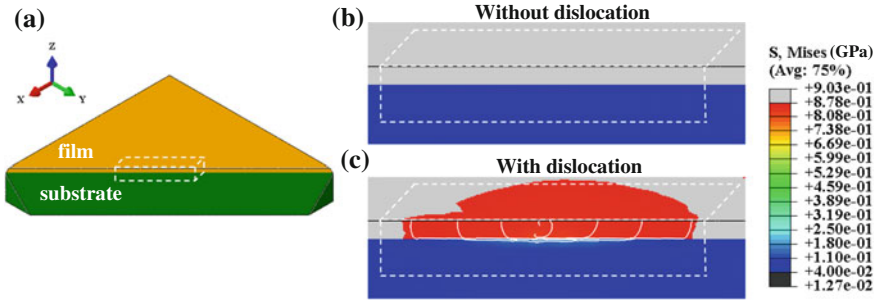

Fig. 2.25 **a** (111) plane cross-sectional view showing the concerned region enclosed by *dotted lines* for film with thick substrate; **b–c** Mises stress field in the concerned region labeled in (**c**) before and after dislocation source operation, respectively. The *white solid lines* in (**c**) represent the dislocation lines, which corresponds to Fig. 2.23j. Reprinted from Ref. [41], Copyright 2015, with permission from Elsevier

2.3 Summary

This chapter describes the discrete dislocation dynamics (DDD) and discrete-continuous model (DCM) simulation method. Several key issues in the coupling between DDD and FEM are systematically investigated. The prerequisite for the application of DCM in complex situations is reasonably localizing the discrete plastic strains induced by dislocation slip to the continuum material points. Thus, a detailed evaluation of current regularization methods in DCM is first presented. A novel regularization method is proposed based on the Burgers vector distribution function and swept area, which considers the dependence of regularization parameter on the angle between slip plane and FEM mesh, and shows excellent accuracy.

To apply DCM to gain insight of plasticity at submicron scale, the image force effect and finite strain effect must be properly introduced. First, by introducing stress interpolation, it is found that DCM is able to obtain comparable precise image force with SPM, and introducing SPM to DCM with the aim of correcting the image force will double-count the image force effect. A new hybrid method is also preliminarily proposed to correct the singular image force in DCM.

The algorithmic details to well capture the finite deformation effect by DCM are presented, which include the deformation field transfer method, and the special treatments on the surface-piercing dislocations and slip system rotation. The validation tests are performed to reproduce the rotation of slip plane, the slip step generated by an edge dislocation, and the localized deformation induced by the continuous operation of single arm source in micropillar. The results show that DCM is capable of capturing the localized deformation.

As an application, the improved DCM is applied to investigate the dislocation evolutions in heteroepitaxial thin films. The misfit stress field is calculated by analogizing thermal expansion process. The dependence of dislocation behavior on the thickness of substrate is revealed and their influence on the internal stress field is captured. It shows the advantages of new DCM in the study of internal microstructure evolution and stress field in the complex crystal devices at submicron scale.

References

1. Dunstan DJ, Bushby AJ (2013) The scaling exponent in the size effect of small scale plastic deformation. Int J Plast 40:152–162
2. Uchic MD, Dimiduk DM, Florando JN, Nix WD (2004) Sample dimensions influence strength and crystal plasticity. Science 305:986–989
3. Hu JQ, Liu ZL, Cui YN, Wang ZJ, Shan ZW, Zhuang Z (2014) Sensitive material behavior: theoretical model and experiment for compression collapse of gold particles at submicron scale. J Appl Mech 81(9):091007. doi:10.1115/1.4027916
4. Zhou C, Beyerlein IJ, LeSar R (2011) Plastic deformation mechanisms of fcc single crystals at small scales. Acta Mater 59(20):7673–7682

5. Csikor FF, Motz C, Weygand D, Zaiser M, Zapperi S (2007) Dislocation avalanches, strain bursts, and the problem of plastic forming at the micrometer scale. Science 318(5848):251
6. Cui YN, Lin P, Liu ZL, Zhuang Z (2014) Theoretical and numerical investigations of single arm dislocation source controlled plastic flow in FCC micropillars. Int J Plast 55:279–292
7. Zhou C, LeSar R (2012) Dislocation dynamics simulations of plasticity in polycrystalline thin films. Int J Plast 30:185–201
8. Espinosa HD, Panico M, Berbenni S, Schwarz K (2006) Discrete dislocation dynamics simulations to interpret plasticity size and surface effects in freestanding FCC thin films. Int J Plast 22(11):2091–2117
9. Devincre B, Madec R, Monnet G, Queyreau S, Gatti R, Kubin L (2011) Modeling crystal plasticity with dislocation dynamics simulations: the 'microMegas' code. Mechanics of nano-objects. Presses de l'Ecole des Mines de Paris, Paris, pp 81–100
10. Gao Y, Zhuang Z, Liu ZL, Zhao XC, Zhang Z (2010) Characteristic sizes for exhaustion-hardening mechanism of compressed Cu single-crystal micropillars. Chin Phys Lett 27(8):086103
11. Gao Y, Liu ZL, You XC, Zhuang Z (2010) A hybrid multiscale computational framework of crystal plasticity at submicron scales. Comput Mater Sci 49:672–681
12. Liu ZL, Liu XM, Zhuang Z, You XC (2009) A multi-scale computational model of crystal plasticity at submicron-to-nanometer scales. Int J Plast 25(8):1436–1455
13. Gao Y (2011) Discrete Dislocation Mechanism on Submicro-crystal Plasticity, PhD thesis of Tsinghua University
14. Liu ZL (2009) The Investigation of Crystal Plasticity at Microscale by Discrete Dislocation and Nonlocal Theory. PhD thesis of Tsinghua University
15. Nadgornyi E (1998) Progress in materials science, dislocation dynamics and mechanical properties, vol 31. Pergamon Press, Oxiford
16. Hirth JP, Lothe J (1982) Theory of dislocations. Wiley, New York, p 857
17. Liu XH, Schwarz KW (2005) Modelling of dislocations intersecting a free surface. Modell Simul Mater Sci Eng 13:1233–1247
18. Rhee M, Zbib HM, Hirth JP, Huang H, Rubia T (1998) Models for long-/short-range interactions and cross slip in 3D dislocation simulation of BCC single crystals. Modell Simul Mater Sci Eng 6:467–492
19. Bulatov VV, Cai W (2006) Computer simulations of dislocations. Oxford University Press, New York
20. Groh S, Zbib HM (2009) Advances in discrete dislocations dynamics and multiscale modeling. J Eng Mater Technol 131:041209
21. Madec R, Devincre B, Kubin LP (2002) Simulation of dislocation patterns in multislip. Scr Mater 47(10):689–695
22. Motz C, Weygand D, Senger J, Gumbsch P (2009) Initial dislocation structures in 3-D discrete dislocation dynamics and their influence on microscale plasticity. Acta Mater 57 (6):1744–1754
23. Rao SI, Dimiduk DM, Parthasarathy TA, El-Awady J, Woodward C, Uchic MD (2011) Calculations of intersection cross-slip activation energies in fcc metals using nudged elastic band method. Acta Mater 59(19):7135–7144
24. Wang ZQ, Beyerlein IJ, LeSar R (2007) The importance of cross-slip in high-rate deformation. Modell Simul Mater Sci Eng 15:675–690
25. Wei H, Wei Y (2012) Interaction between a screw dislocation and stacking faults in FCC metals. Mater Sci Eng A 541(15):38–44
26. Püschl W (2002) Models for dislocation cross-slip in close-packed crystal structures: a critical review. Prog Mater Sci 47(4):415–461. doi:http://dx.doi.org/10.1016/S0079-6425(01)00003-2
27. Cui YN, Liu ZL, Zhuang Z (2013) Dislocation multiplication by single cross slip for FCC at submicron scales. Chin Phys Lett 30(4):046103
28. Devincre B (1996) Meso-scale simulation of the dislocation dynamics. NATO ASI Ser E Appl Sci-Adv Study Inst 308:309–324

29. Kubin LP, Canova G, Condat M, Devincre B, Pontikis V, Bréchet Y (1992) Dislocation microstructures and plastic flow: a 3D simulation. Solid State Phenom 23:455–472
30. Groh S, Marin EB, Horstemeyer MF, Zbib HM (2009) Multiscale modeling of the plasticity in an aluminum single crystal. Int J Plast 25(8):1456–1473
31. Zbib HM, de la Rubia TD, Bulatov V (2002) A multiscale model of plasticity based on discrete dislocation dynamics. J Eng Mater Technol 124(1):78–87
32. Van der Giessen E, Needleman A (1995) Discrete dislocation plasticity: a simple planar model. Modell Simul Mater Sci Eng 3(5):689–735
33. Po G, Mohamed MS, Crosby T, Erel C, El-Azab A, Ghoniem NM (2014) Recent progress in discrete dislocation dynamics and its applications to micro plasticity. JOM 66(10):2108–2120. doi:10.1007/s11837-014-1153-2
34. Zhou C, Biner SB, LeSar R (2010) Discrete dislocation dynamics simulations of plasticity at small scales. Acta Mater 58(5):1565–1577
35. El-Awady JA, Bulent Biner S, Ghoniem NM (2008) A self-consistent boundary element, parametric dislocation dynamics formulation of plastic flow in finite volumes. J Mech Phys Solids 56(5):2019–2035
36. Lemarchand C, Devincre B, Kubin LP (2001) Homogenization method for a discrete-continuum simulation of dislocation dynamics. J Mech Phys Solids 49(9):1969–1982
37. Vattré A, Devincre B, Feyel F, Gatti R, Groh S, Jamond O, Roos A (2013) Modelling crystal plasticity by 3D dislocation dynamics and the finite element method: the discrete-continuous model revisited. J Mech Phys Solids 63:491–505
38. Zbib HM, de la Rubia TD (2002) A multiscale model of plasticity. Int J Plast 18(9): 1133–1163
39. Chen Q, Biner B (2006) Evolution and interaction of dislocations in intermetallics: fully anisotropic discrete dislocation dynamics simulations. MRS online proceedings library 980, null-null (2006). doi:10.1557/PROC-980-0980-II05-16
40. O'day MP, Curtin WA (2005) Bimaterial interface fracture: a discrete dislocation model. J Mech Phys Solids 53(2):359–382
41. Cui YN, Liu ZL, Zhuang Z (2015) Quantitative investigations on dislocation based discrete-continuous model of crystal plasticity at submicron scale. Int J Plast 69:54–72
42. Weinberger CR, Cai W (2007) Computing image stress in an elastic cylinder. J Mech Phys Solids 55(10):2027–2054
43. Uchic MD, Shade PA, Dimiduk DM (2009) Plasticity of micrometer-scale single crystals in compression. Annu Rev Mater Res 39:361–386
44. Dimiduk DM, Uchic MD, Parthasarathy TA (2005) Size-affected single-slip behavior of pure nickel microcrystals. Acta Mater 53(15):4065–4077
45. Deshpande VS, Needleman A, Van der Giessen E (2003) Finite strain discrete dislocation plasticity. J Mech Phys Solids 51(11–12):2057–2083. doi:10.1016/j.jmps.2003.09.012
46. Akarapu S, Zbib HM, Bahr DF (2010) Analysis of heterogeneous deformation and dislocation dynamics in single crystal micropillars under compression. Int J Plast 26(2):239–257
47. Mura T (1987) Micromechanics of defects in solids, vol 3. Springer, Berlin
48. Cai W, Arsenlis A, Weinberger C, Bulatov V (2006) A non-singular continuum theory of dislocations. J Mech Phys Solids 54(3):561–587
49. Tang M, Cai W, Xu G, Bulatov VV (2006) A hybrid method for computing forces on curved dislocations intersecting free surfaces in three-dimensional dislocation dynamics. Modell Simul Mater Sci Eng 14:1139
50. Yoffe EH (1961) A dislocation at a free surface. Phil Mag 6(69):1147–1155
51. Li JCM (1964) Stress field of a dislocation segment. Phil Mag 10(108):1097–1098
52. Crone JC, Chung PW, Leiter KW, Knap J, Aubry S, Hommes G, Arsenlis A (2014) A multiply parallel implementation of finite element-based discrete dislocation dynamics for arbitrary geometries. Modell Simul Mater Sci Eng 22(3):035014. doi:035014/0965-0393/22/3/035014
53. Asaro RJ, Rice J (1977) Strain localization in ductile single crystals. J Mech Phys Solids 25 (5):309–338

54. Rao SI, Dimiduk DM, Tang M, Uchic MD, Parthasarathy TA, Woodward C (2007) Estimating the strength of single-ended dislocation sources in micron-sized single crystals. Philos Mag 87(30):4777–4794
55. Wang YU, Jin YM, Khachaturyan AG (2003) Phase field microelasticity modeling of dislocation dynamics near free surface and in heteroepitaxial thin films. Acta Mater 51 (14):4209–4223. doi:10.1016/s1359-6454(03)00238-6
56. Shen YL (2008) Externally constrained plastic flow in miniaturized metallic structures: a continuum-based approach to thin films, lines, and joints. Prog Mater Sci 53(5):838–891. doi:10.1016/j.pmatsci.2008.03.001
57. Newberger M (ed) (1971) Handbook of electronic materials group IV semiconducting materials. IFI/Plenum, New York

http://www.springer.com/978-981-10-3031-4

The Investigation of Plastic Behavior by Discrete Dislocation Dynamics for Single Crystal Pillar at Submicron Scale

Cui, Y.

2017, XIV, 131 p. 71 illus., 67 illus. in color., Hardcover
ISBN: 978-981-10-3031-4